Front. Struct. Civ. Eng. 2023, 17(10): 1477–1501
https://doi.org/10.1007/s11709-023-0966-x

RESEARCH ARTICLE

Influence of advanced engineering measures on displacement and stress field of surrounding rock in tunnels crossing active strike-slip faults

Hui ZHOU[a,b], Jiancheng XIAO[a,b*], Manchao HE[c,d], Jingjing LU[a,b*], Zhigang TAO[c,d], Futong XU[a,b], Congcong HOU[a,b]

[a] *State Key Laboratory of Geomechanics and Geotechnical Engineering, Institute of Rock and Soil Mechanics, Chinese Academy of Sciences, Wuhan 430071, China*

[b] *School of Engineering Science, University of Chinese Academy of Sciences, Beijing 100049, China*

[c] *State Key Laboratory for Geomechanics and Deep Underground Engineering, China University of Mining and Technology, Beijing 100083, China*

[d] *School of Mechanics and Civil Engineering, China University of Mining and Technology, Beijing 100083, China*

[*] *Corresponding authors. E-mails: xiaojiancheng19@mails.ucas.ac.cn; jjlu@whrsm.ac.cn*

ABSTRACT Based on significant improvements in engineering materials, three advanced engineering measures have been proposed—super anchor cables, high-strength concrete anti-fault caverns, and grouting modification using high-strength concrete-to resist fault dislocation in the surrounding rock near tunnels crossing active strike-slip faults. Moreover, single- or multiple-joint advanced engineering measures form the local rock mass-anti-fault (LRAF) method. A numerical method was used to investigate the influence of LRAF methods on the stress and displacement fields of the surrounding rock, and the anti-fault effect was evaluated. Finally, the mechanism of action of the anchor cable was verified using a three-dimensional numerical model. The numerical results indicated that the anchor cable and grouting modification reduced the displacement gradient of the local surrounding rock near the tunnels crossing fault. Furthermore, anchor cable and grouting modifications changed the stress field of the rock mass in the modified area. The tensile stress field of the rock mass in the modified anchor cable area was converted into a compressive stress field. The stress field in the modified grouting area changed from shear stress in the fault slip direction to tensile stress in the axial tunnel direction. The anti-fault cavern resisted the dislocation displacement and reduced the maximum dislocation magnitude, displacement gradient, and shear stress. Among the three advanced engineering measures, the anchor cable was the core of the three advanced engineering measures. An anchor cable, combined with other LRAF measures, can form an artificial safety island at the cross-fault position of the rock mass to protect the tunnel. The research results provide a new supporting idea for the surrounding rock of tunnels crossing active strike-slip faults.

KEYWORDS anti-fault effect, engineering measures, LRAF method, stress and displacement field, tunnel-crossing active faults

1 Introduction

An active strike-slip fault is a horizontal dislocation fault formed by two rock masses under the action of horizontal shear tectonic stress (Fig. 1(a)). The geological history of displacement-distribution patterns is preserved [1,2], based on the strike-slip and creep displacement modes. Dislocation along a strike-slip fault is represented by an apparent suddenness, periodicity, strong instantaneous energy release, wide range of influence, and large instantaneous destructive force. For example, during the San Francisco earthquake in 1906, the surrounding rock

Article history: Received Sep 12, 2022; Accepted Dec 5, 2022

in the Wrights tunnel crossing the San Andreas fault zone in the United States was a staggering 1.7–1.8 m [3]. During the Wenchuan earthquake in 2008, the surrounding rock in the Youyi tunnel crossing the Longmenshan fault zone in China was 0.8 m (Fig. 1(b)) [4]. However, creep fault dislocation is slow and continuous, and the dislocation displacement accumulates annually. For example, the Claremont tunnel across the Hayward active fault slipped by 330 mm over 79 years [5]. The San Andreas et al. [6,7], Hayward et al. [8,9], Jinshajiang, and Ganzi–Yushu [10] fault zones in China are typical strike-slip creep active faults that can reach meter-level dislocations during the service life of a tunnel project. Because the supporting structure of the tunnel has a weaker ability to resist shear than axial deformations, the dislocation of both sides of the rock mass in the active fault zone causes movement and vibration of the surrounding rock. This causes severe fault disasters at tunnel crossings [11–13]. Moreover, this poses significant challenges for the safe and stable operation of tunnel projects. Therefore, the design and construction of tunnel lines should avoid crossing active faults as much as possible.

In recent years, many tunnel projects have been built on the edge of the Asia–Europe plate in southwest China to alleviate transportation and resource shortages in the western region of China. Among these, some tunnels inevitably cross-active fault zones. For example, the Sichuan–Tibet Railway, which is currently under construction, is expected to cross the Xianshuihe and Litang fault zones, with average annual dislocation displacements of 10 and 4–5 mm, respectively. Therefore, research on anti-fault measures for active fault tunnel crossings is crucial.

Domestic and foreign studies on the safety of active fault tunnel crossings have focused on the displacement pattern, stress-field distribution of the surrounding rock, deformation and internal force of the tunnel, support measures, and support effect evaluation. Some researchers have found that the displacement pattern of the tunnel axis exhibits an S-shaped curve in active fault dislocations [14–17]. In addition, some scholars have performed experiments and simulations to study the influence of the active fault dislocation-displacement mode on tunnel deformation and internal force distribution. The results indicate that under fault dislocation, the affected range of the lining is mainly concentrated near the fault fracture zone [18,19], and the peak stress in the tunnel appears at the junction of the fault fracture zone, hanging wall, and footwall [20,21]. In addition, some scholars have studied the stress-field distribution pattern of the surrounding rock in tunnels crossing active faults [22–24]. Additionally, based on research results on displacement patterns and stress-field distributions, some scholars have proposed an advanced support method to improve the tunnel-support structure. Advanced support methods include hinged linings combined with flexible concrete [25–27], lining segments, and open pipes in tunnel [28–31]. In addition, supporting methods have been proposed to improve the mechanical properties of tunnel surrounding rock, such as applying a buffer layer between the lining and the surrounding rock or grouting reinforcement in the weak surrounding rock [32]. Given these tunnel anti-fault measures, researchers have studied the principle of a supporting structure containing fault displacement [33–36] and evaluated its supportive effect [29,37].

In summary, most current research is based on experimental and numerical analyses. The cross-active fault tunnel displacement pattern, deformation, internal force of the tunnel, and stress distribution of the surrounding rock mass are thoroughly investigated, and feasible tunnel support and anti-fault schemes are proposed. Among them, the anti-fault method of the tunnel primarily considers the improvement of the tunnel-support pattern and the hinged structure of the lining. Anti-fault refers to resisting the dislocation displacement of the active faults. However, for some active faults with enormous annual average dislocations that cannot be bypassed, it remains challenging to adopt current

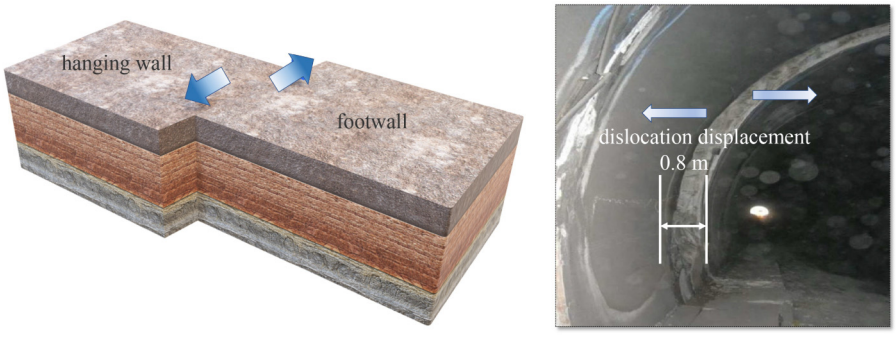

Fig. 1 rock mass movement patterns of active strike-slip and tunnel fault disasters: (a) rock mass dislocation pattern of strike-slip fault; (b) dislocation of the Youyi tunnel lining across the Longmenshan fault zone reached 0.8 m during the Wenchuan earthquake [4].

engineering measures to resist fault dislocations of tunnel crossings. Therefore, advanced engineering measures should be implemented to prevent fault dislocations. With remarkable progress in material science, the emergence of high-performance techniques and ultrahigh-performance engineering materials has provided novel ideas for designing tunnel anti-fault methods such as anchor cables [38–40], anti-fault caverns [41–43], and rock mass grouting modifications [44–46]. Compared to improving the anti-fault measures of tunnel-supporting structures, these advanced engineering measures can change the maximum dislocation magnitude and bearing capacity of the rock mass. Additionally, the cost is lower, action time is longer, and construction is easier.

Single or multiple-joint local rock mass-anti-fault (LRAF) methods have been proposed using three advanced engineering measures—sizable constant resistance force and large deformation ability anchor cables, ultrahigh-strength concrete anti-fault caverns, and local surrounding rock grouting modifications using high-strength concrete. Furthermore, the Yuanmou–Luzhijiang fault zone was considered the benchmark for this study. The influence of three advanced engineering measures and their combinations on the stress and displacement fields of the surrounding rock were investigated using a numerical method, and the anti-fault effect of each scheme was evaluated. In addition, the application scenarios of the LRAF methods were combined with research results.

2 Methodology

2.1 Basic principle of the local rock mass-anti-fault method

There are several ways to limit the relative movement of two objects, such as binding two objects with ropes or wires, installing pin structures on sliding surfaces, or to reinforce sliding surfaces with glue. However, it is implausible to restrict or reduce fault dislocations in this manner. The two sides of the active fault rock mass extend thousands of kilometers along the strike, and the constructed tunnel, and the supporting structure is negligible compared with the scale of the active fault structure. Therefore, it was impractical to limit the dislocation displacement of two large rock masses in an active fault structure by using artificial systems. However, the rock masses on both sides of the fault could be regarded as semi-infinite spaces. This is a natural stress- and strain-absorbing container. At the position where the tunnel passes through the fault dislocation area, within the local range of 30–50 m relative to the overall scale of the tunnel, advanced engineering measures were used to resist dislocation displacement from the enormous fault sliding surface within a specific period. The stress and dislocation displacement concentrated on the local fault sliding surface were dispersed into the stable surrounding rock on both sides of the fault. This idea seems feasible.

With the development of material science, the strength of materials (such as anchor cables and concrete) has dramatically improved, and surrounding rock mass reinforcement technology has also made progress. A negative Poisson's ratio (NPR) material anchor cable was developed with a maximum constant resistance of 850 kN and maximum tensility between 2 and 4 m [47–49]. Researchers have developed ultrahigh-strength concrete, such as C130 and ultra high-performance concrete , with strengths of 130–150 MPa or higher [50–52]. In addition, with the development of rock grouting technology, the strength index of broken rock masses has significantly improved [53,54]. Most importantly, these technologies provide possibilities for the implementing of the LRAF method.

Therefore, the LRAF method was proposed for tunnels across active faults. This method uses three advanced engineering measures: local rock mass modification through anchor cable bundles or giant anchor cables, local rock mass reinforcement through high-strength-anti-fault caverns, and local rock mass grouting modification through high-strength concrete. Based on to the fault movement characteristics and surrounding rock conditions, an advanced engineering measure or a combination of various engineering measures was selected as the LRAF method. Before or during construction, engineering measures of LRAF are deployed in the rock mass at the fault fracture zone and fault-affected area to improve the integrity and strength of weak or fractured rock masses or to replace inefficient and fractured rock masses with ultrahigh-strength materials. Thus, the maximum dislocation magnitude and displacement gradient at the local position of the tunnel crossing are reduced.

As shown in Fig. 2(a), several giant anchor cables with high constant resistance and high tensility capacity were arranged in the rock mass in the vertical direction of the tunnel crossing the fault position. The two ends of the anchor cables were anchored to a stable rock mass at the hanging wall and footwall of the fault. The arrangement of the anchor cable body has an angle of 45° with the fault fracture zone plane to minimize the shear effect of the anchor cable on the rock mass dislocation and give full play to the high constant resistance advantage of the anchor cable [47]. The rock mass pulled out the anchor cable when fault dislocation occurred. The pretension anchor cable generates a constant resistance to pull the rock mass in the anti-fault area and transfers the concentrated dislocation displacement to the stable surrounding rock of the double plates through the prominent deformation characteristics of the anchor

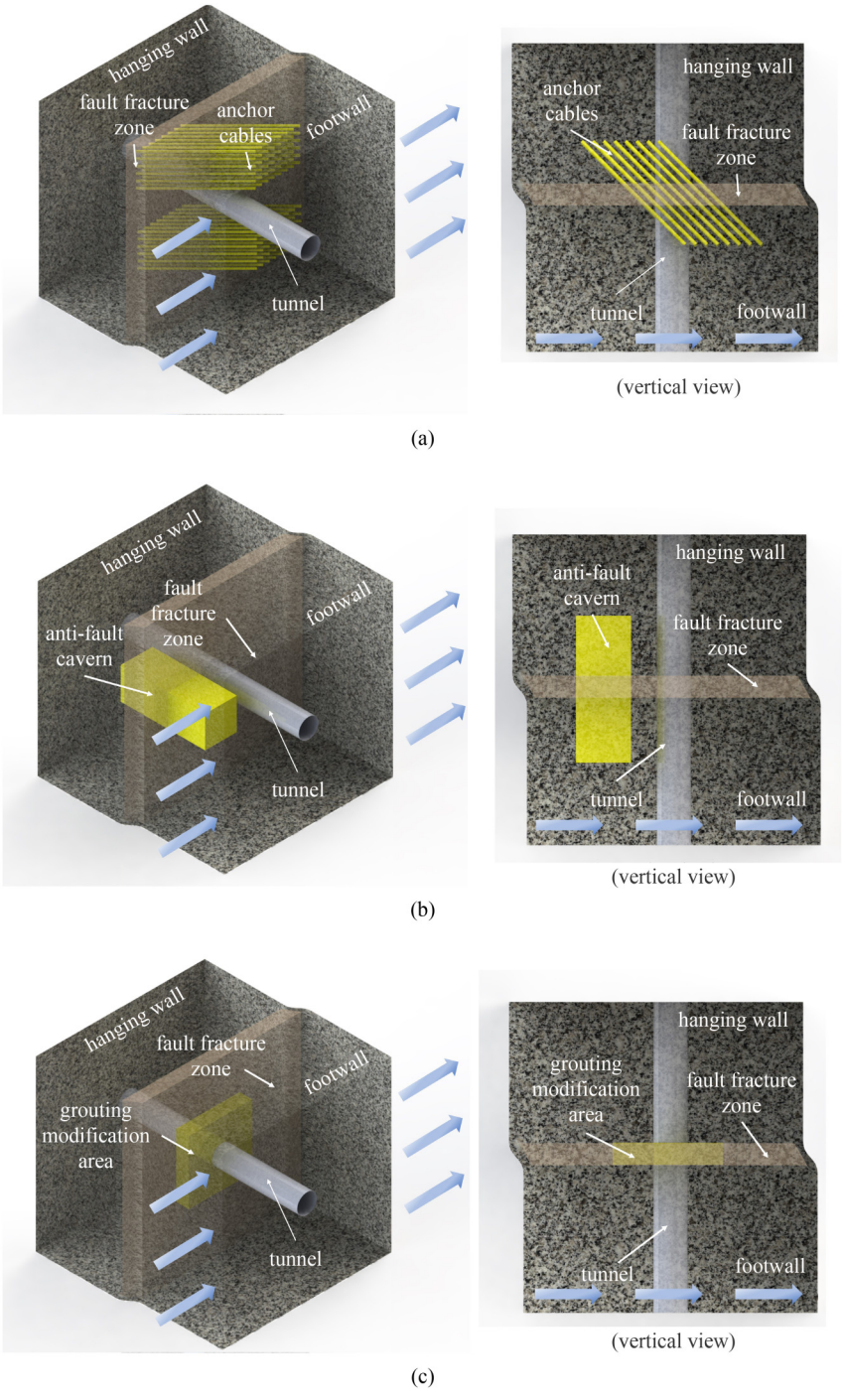

Fig. 2 LRAF for tunnels crossing active faults: (a) anchor cables; (b) anti-fault caverns; (c) local rock mass grouting modification.

cable. This process reduces the dislocation concentration (displacement gradient) in the anti-fault area. This disperses the concentrated large deformation into a small local deformation, thus creating better support conditions for the tunnels. In principle, the anchor cable binds two plates of the fault rock mass, similar to a bundle of ropes. However, it is worth noting that the range of influence and action time of the anchor cable for reducing the displacement gradient is limited, depending on its constant resistance force value and maximum deformation ability. In tunnel engineering, the action time of an anchor cable should be longer than the service life of the tunnel.

As shown in Fig. 2(b), the anti-fault cavern structure commonly used in water conservancy and hydropower fields is introduced into the LRAF measures [55], which are set in the rock mass on one or both sides of the fault dislocation direction of the tunnel. The layout of the anti-fault cavern is orthogonal to the plate of the fault fracture zone, and the two ends of the anti-fault cavern are in a

stable rock mass on both scales of the fault. Simultaneously, a steel reinforcement cage was inserted into the anti-fault cavern and injected into high-strength or ultrahigh-strength concrete to form one or more pin structures in the fault fracture zone. When a fault dislocation occurs, the anti-fault cavern uses the stiffness difference between its structure and the rock mass to block and absorb the dislocation displacement. Within their service life, the maximum dislocation displacement and dislocation displacement of the tunnel across the fault fracture zone were reduced.

In addition, as shown in Fig. 2(c), using rock mass-grouting-reinforcement technology [56], high-strength or ultrahigh-strength concrete slurry was injected into the fractured rock mass of the tunnel across the fault position and within a specific range. After the concrete slurry solidified in the rock mass joint network, a high-strength concrete network was formed to improve the strength and stiffness of the rock mass in the region. When fault dislocation occurs, the grouting rock mass is similar to the glue that sticks together with the rock mass of the hanging wall and footwall. At the same time, the stiffness of the grouting rock mass is much larger than that of the broken rock mass and close to that of the hanging wall and footwall stable surrounding rock. Thus, the concentrated dislocation displacement was dispersed into the stable rock mass, reducing the dislocation displacement gradient.

2.2 Methodology of numerical analysis

2.2.1 Numerical modeling and boundary conditions

Based on the LRAF method of the tunnel, as shown in Fig. 3, under the condition of distributed and concentrated strike-slip faults, a horizontal range of 300 m in the vertical direction of the tunnel surrounding rock was taken as the section. We then established a single and multi-mean joint LRAF numerical model and set its control group for a total of 14 groups of models. Figures 3(a)–3(d) and 3(e)–3(h) show the numerical models of the single LRAF measures for the distributed and concentrated strike-slip faults, respectively. Figures 3(i)–3(l) and 3(m)–3(p) show the numerical models of LRAF measures for multi-engineering combinations for distributed and concentrated strike-slip faults, respectively. The rock mass model adopted triangular elements with a unit size of 3 m, and the middle of the model corresponded to the area in which the tunnel passed.

Simultaneously, three monitoring lines were set along the *Y*-direction in the numerical model of the surrounding rock. The *X*-direction displacement of the surrounding rock with and without LRAF was monitored, and the displacement gradient was calculated. Based on several numerical simulation tests, the influence of dislocations on the rock mass can be ignored when the distance from the fault fracture zone is greater than 100 m. Therefore, the length of the monitoring line was 200 m (100 m in the hanging wall plate and 100 m in the footwall plate), and the distance between each monitoring point was 5 m, for a total of 42 monitoring points.

The following numerical simulation process was designed according to the LRAF method principle, as shown in Fig. 4.

The first step was to initialize the stress field and balance the model.

The second step is to impose a fixed boundary condition on the hanging wall rock mass. Moreover, a velocity boundary condition in the same direction was set on the three boundaries of the footwall rock mass to simulate fault dislocation, similar to the rigid-body translation. Simultaneously, the existing stress boundary of the model continues to interact with the velocity boundary condition to maintain the stress field of the model until the fault fracture zone reaches a complete plastic state, and the model calculates the balance.

The third step is to apply the anchor cable element and reinforcement area at both ends and then use the anchor cable pretension. If the model does not contain an anchor cable, skip this step. Owing to the anchor at both ends of the anchor cable, the hanging wall and footwall plates continued to stagger to pull the anchor cable to apply pretension. The calculation step for the anchor cable before reaching the pretension setting value was not included in the final calculation results. The formal calculation begins after the pretension value is obtained.

The fourth step was to apply the other LRAF measures. After the anchor cable pretensions, were used, other boundary conditions were applied.

The fifth step calculated the footwall rock mass dislocation to a predetermined dislocation magnitude.

2.2.2 Parameters

To ensure the coordination of the numerical model parameters, the mechanical parameters of the surrounding rock of the Yuanmou–Luzhijiang fault zone in the Yunnan Province of China were used to establish an idealized numerical model. The Yuanmou–Luzhijiang fault zone is a representative shear strike-slip fault zone. According to relevant geological survey reports, the fault characteristics include left-lateral slip rates of 4.25 mm/a. Moreover, the rock mass model adopted the Mohr–Coulomb ideal elastic–plastic constitutive model, which can better simulate the creep characteristics of the fault fracture zone. The simplified mechanical parameters of the surrounding rock are listed in Table 1.

In the calculation, it was assumed that the service life of the tunnel was two hundred years. According to the

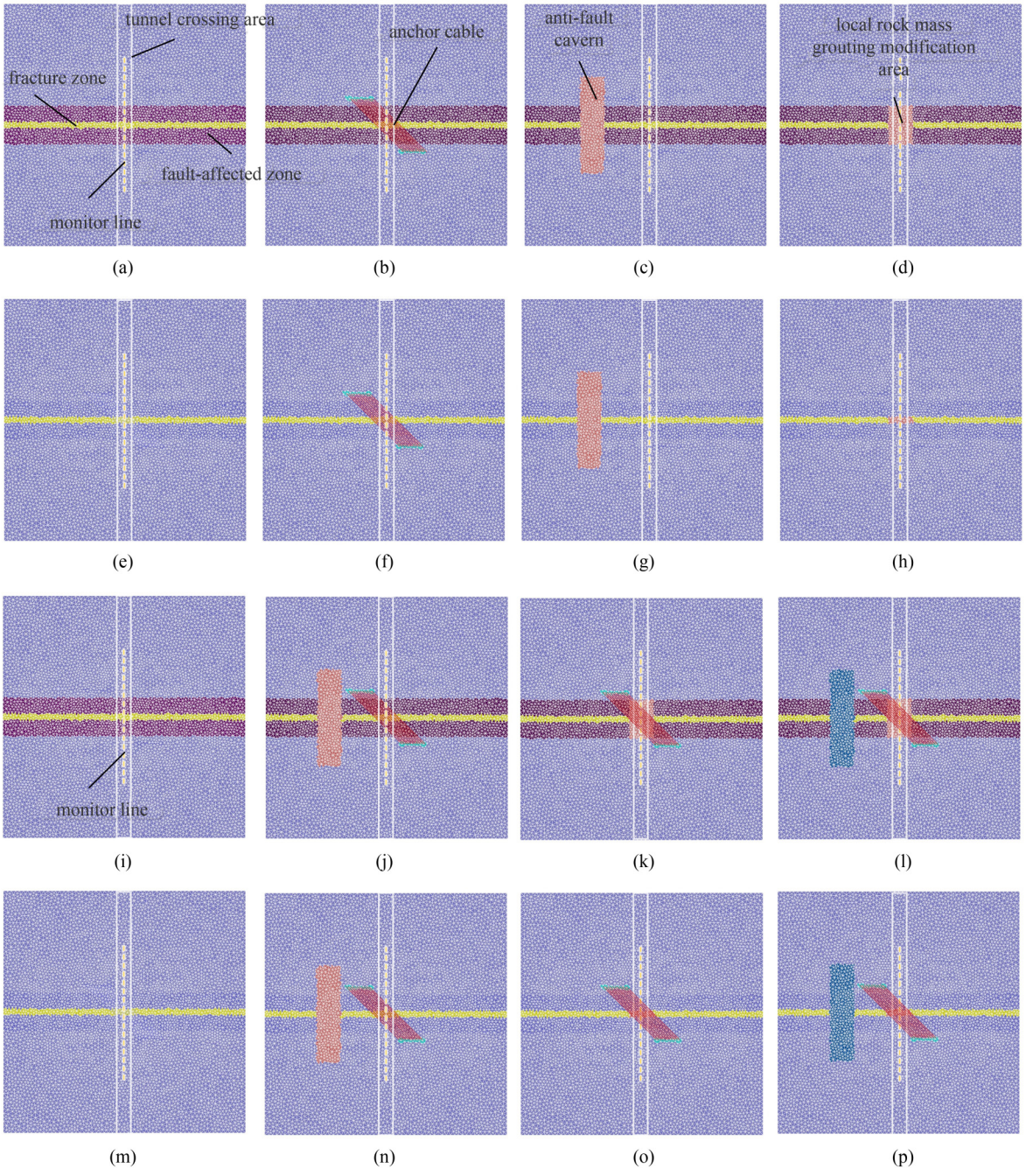

Fig. 3 Numerical models of different LRAF measures for distributed and concentrated displacement patterns: (a) control group (distributed); (b) anchor cable (distributed); (c) anti-fault cavern (distributed); (d) local grouting modification (distributed); (e) control group (concentrated); (f) anchor cable (concentrated); (g) anti-fault cavern (concentrated); (h) local grouting modification (concentrated); (i) control group (distributed); (j) anchor cable and anti-fault cavern (distributed); (k) anchor cable and local grouting modification (distributed); (l) three measures combination (distributed); (m) control group (concentrated); (n) anchor cable and anti-fault cavern (concentrated); (o) anchor cable and local grouting modification (concentrated); (p) three measures combination (concentrated).

maximum annual average slip rate of the fault, the maximum dislocation displacement was 1 m after applying LRAF measures. The dislocation rate was 1×10^{-8} m per step after many attempts to avoid the dynamic effect of the rock mass and to better simulate the characteristics of rock mass creep and dislocation. The width of the concentrated fault fracture zone was 7 m, and the width of the distributed fault fracture zone was consistent with that of the concentrated structure. The width of the distributed fault-affected zone was 20 m and there was no fault-affected zone in the concentrated fault zone. The dimensions and parameters of other numerical models are presented in Fig. 5 and Table 2.

In Table 2, D_{Cable} denotes the anchor cable diameter;

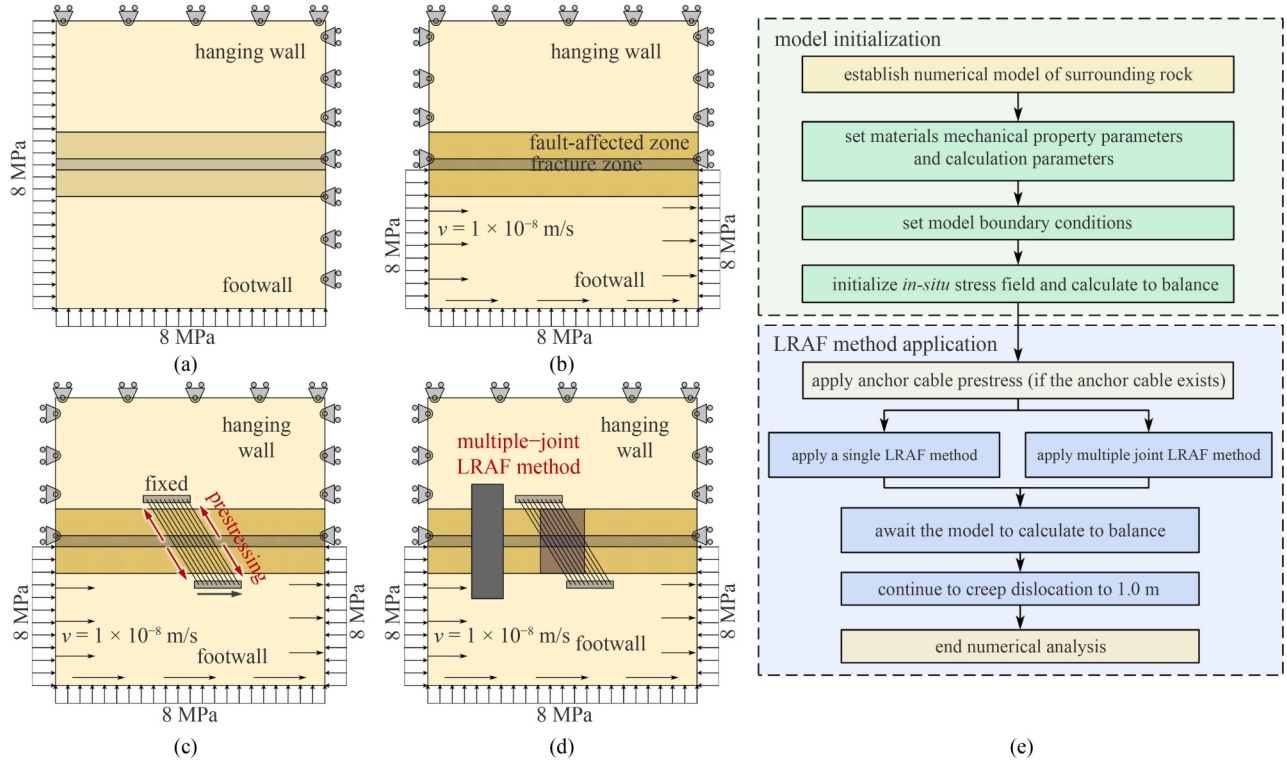

Fig. 4 Numerical simulation steps of local anti-fault measures: (a) initialized *in situ* stress field; (b) formation of geological environment of active strike-slip fault; (c) pretension of anchor cable applied if the model contains anchor cable; (d) continue to creep dislocation to the preset displacement with LRAF measures; (e) numerical flow chart.

Table 1 Conventional mechanical parameters of metal specimens

fault geological division	ρ (kg/m^3)	E (GPa)	μ	c (MPa)	φ (°)	tensile strength (MPa)	*In situ* stress (MPa)
fracture zone	2500	0.5	0.35	0.3	20	0.1	8
fault-affected zone	2600	2.0	0.29	1.3	32	0.3	
stable surrounding rock mass	2700	20.0	0.27	15.0	35	2.0	
reinforcement area	2500	50.0	0.20	50.0	55	100.0	

L_{Cable} is the length of the anchor cable; α is the angle between the anchor cable layout axis and the fault dislocation direction; c, φ, and k are the anchor area cohesion, internal friction angle, and stiffness, respectively; σ_{pre} is the magnitude of the pretension force of the anchor cable; $H_{\text{R-A}}$ is the distance between the anchor cable end reinforcement area boundary and boundary of the fault-affected zone; and $H_{\text{C-A}}$ is the distance between the boundary of the anti-fault cavern and the anchor cable.

3 Numerical analysis of a single local rock mass-anti-fault measure

3.1 Influence on the displacement field of the surrounding rock

After the calculation, the displacement magnitude nephogram in the X-direction of the model and the displacement curve in the X-direction of the axial position monitoring point of the tunnel when the fault dislocation displacement was 1.0 m are obtained through postprocessing. As shown in Figs. 6(a) and 6(e), when no LRAF measures were adopted, the dislocation displacement of the fault was concentrated in the rock mass of the fault fracture zone with low strength and stiffness. The dislocation-displacement concentration area showed an apparent belt shape, in which the dislocation displacement of the concentrated fault was more concentrated than that of the distributed fault. Furthermore, as shown in Figs. 6(b)–6(d) and 6(f)–6(h), the LRAF measures had a considerable influence on the displacement field in the rock surrounding the strike-slip active fault. With the application of LRAF measures, the dislocation displacement in the surrounding rock of the fault fracture zone began to spread to the surrounding rock of the hanging wall and footwall plates, and the boundary of the dislocation displacement changed from belt-type to spindle or ellipse. It can also be observed from Fig. 6 that

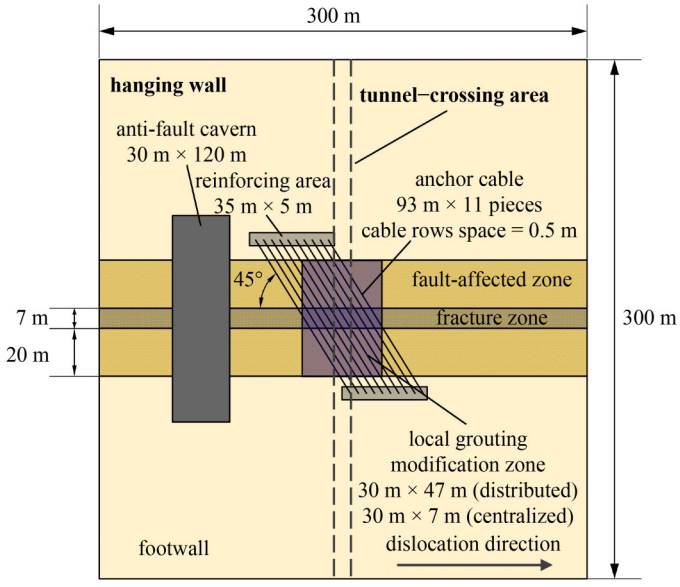

Fig. 5 Generalized model of LRAF measures.

Table 2 LRAF measurement parameter

LRAF measure type	size and layout mode	material properties	constitutive model	anchoring parameter
anchor cable	D_{Cable} = 0.08 m L_{Cable} = 93 m α = 45° reinforcing area of both ends of anchor cable 35 m × 5 m $H_{R\text{-}A}$ = 8 m	190 GPa	linear	c = 50 MPa φ = 60° $k = 50 \times 10^9$ Pa·m σ_{pre} = 1000 kN
anti-fault cavern	30 m × 120 m $H_{C\text{-}A} \geqslant 8$ m	50 GPa	linear	–
local grouting modification	30 m × 47 m (distributed) 30 m × 7 m (concentrated)	80% complete rock strength index	linear	–

different LRAF measures have different effects on the displacement field in faults with different displacement patterns.

At the same time, from the X-direction displacement curve in Fig. 6, the displacement of the rock mass of the tunnel axis presents an evident S-type displacement mode. The slope of the displacement curve of the distributed fault near the fracture zone was less than that of the concentrated fault, which conforms to the principle of tunnel displacement mode obtained in the current test and engineering. When no LRAF method exists in the surrounding rock, the dislocation displacement of the rock mass is concentrated in the fault fracture zone, and the X-direction displacement curve maximum slope appears in the fault fracture zone range. When the LRAF methods are used in the surrounding rock, the maximum slope of the X-direction displacement curve in the fault fracture zone range significantly decreases compared with that without the LRAF method. In addition, the maximum slope reduction in the X-direction displacement curve under the distributed fault was more significant than that under the concentrated fault. Notably, when different LRAF methods were adopted, the shapes of the X-direction displacement curves differed.

Figures 6(b) and 6(f) show that the local rock mass modification through the anchor cable significantly influenced the displacement field of the strike-slip active fault rock mass. With an increase in dislocation displacement, the displacement boundary of the dislocation zone transfers to the stable surrounding rock mass, and a diffusion phenomenon occurs. Compared with the concentrated dislocation of the rock mass without LRAF methods (Figs. 6(a) and 6(e)), the dislocation displacement of the fault was more dispersed, and the shape of the dislocation-displacement area changed from belt to shuttle. Combined with the displacement vector diagram analysis, the X-direction displacement value of the anchor cable-modified area in the hanging wall stable rock mass was significantly improved compared to that without LRAF measures. Furthermore, the direction of the displacement vector was deflected from the X-positive to the Y-negative direction. At the same time, the dislocation-displacement curve shows that it begins to transition to the maximum dislocation magnitude when it is 25 m from the fault fracture zone (the fault-affected zone range). In addition,

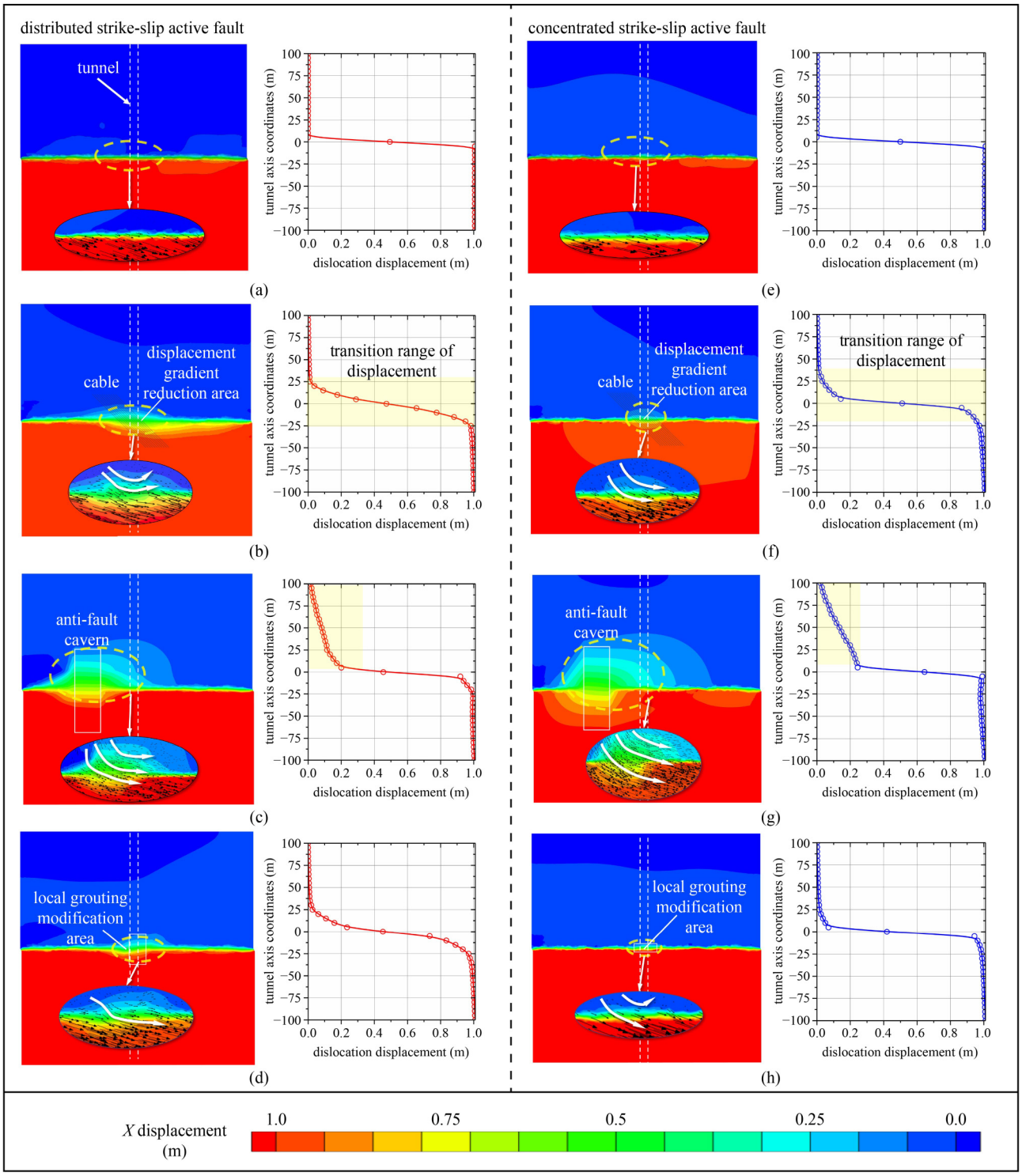

Fig. 6 *X*-direction displacement magnitude and resultant displacement vector of different LRAF measures for distributed and concentrated pattern faults: (a) control group (distributed); (b) anchor cable (distributed); (c) anti-fault cavern (distributed); (d) local grouting modification (distributed); (e) control group (concentrated); (f) anchor cable (concentrated); (g) anti-fault cavern (concentrated); (h) local grouting modification (concentrated).

the displacement slope under distributed faults was smaller than that under concentrated faults, and the displacement transition range under concentrated faults was more extensive (as shown in the highlighted area in the displacement curve in Figs. 6(b) and 6(f)). This phenomenon occurs because the rock mass stiffness in the fault-affected zone in the distributed fault is small, and it is easier to contain displacement. Moreover, both

sides of the fracture zone of the concentrated fault are stable rock masses that require a more extensive range of rock masses to contain fault dislocation displacement.

In addition, there is a small *Y*-negative direction displacement in the rock surrounding the reinforcement area at the upper end of the anchor cable (Fig. 7(a)). Moreover, the maximum dislocation displacement in the modified region of the rock mass of the dislocation plate is significantly reduced (Fig. 7(b)). This phenomenon shows that the anchor cable pulled the hanging wall rock mass movement, resisted the dislocation displacement of the footwall rock mass, and dispersed the concentrated dislocation displacement to the hanging wall and the footwall stable surrounding rock mass. This reduces the displacement gradient of the surrounding rock near the fault dislocation zone. Simultaneously, the most extensive concentrated dislocation displacement is dispersed into small tiny area deformations, which reduces the maximum dislocation displacement of the anchor cable-modified area across the strike-slip active faults.

As shown in Figs. 6(c) and 6(g), the influence of the local reinforcement measures through the anti-fault cavern on the displacement field of the surrounding rock is significantly different from that of the anchor cable. With an increase in the dislocation displacement, the dislocation-displacement boundary in the anti-fault cavern diffuses to the interface between the anti-fault cavern and the stable surrounding rock mass, and the displacement gradient in the local reinforcement area decreases significantly. At the same time, it can be seen from the dislocation-displacement curve that the range of influence of the anti-fault cavern is much larger than that of the anchor cable. The range of influence was twice that of the axial length (*Y*-direction) of the anti-fault cavern. Moreover, the influence of the anti-fault cavern on the rock mass of the hanging wall rock mass is more significant than that of the footwall rock mass. Additionally, the displacement gradient in the surrounding rock on the side of the dislocation direction outside the anti-fault cavern decreased significantly, and the maximum dislocation displacement decreased.

Moreover, the *Y*-direction displacement contour and vector diagram (Fig. 8(a)) show that the anti-fault cavern changed the dislocation direction of the surrounding rock mass. Furthermore, it causes dislocation displacement in the *X*-direction of the hanging wall rock mass to deflect in the *Y*-negative direction. The anti-fault cavern blocked the partial dislocation displacement. Dislocation displacement was transferred to the stable surrounding rock of the hanging wall and footwall (Fig. 8(b)) to reduce the displacement gradient of the local rock mass reinforcement area.

As shown in Figs. 6(b) and 6(h), when grouting modification measures were adopted in the local fracture rock mass zone, the supporting capacity of the local fracture zone rock mass improved. The boundary of the dislocation displacement was transferred to the stable surrounding rock, and the displacement gradient of the grouting modification area decreased significantly. The dislocation-displacement curve of the local reinforcement with an anti-fault cavern was similar to that of an anchor cable, and the influence range of the local reinforcement area was equal to the width of the fault-affected zone. The slope of the dislocation-displacement curve of the fracture zone range in the distributed strike-slip fault is lower than that in the concentrated fault. In addition, the displacement and displacement vector diagram in the *Y*-direction (Fig. 9(a)) show that the rock mass used the LRAF method of the anti-fault cavern and was similar to the LRAF method of the anchor cable. In addition, the grouting reinforcement area changed the direction of the dislocation displacement of the surrounding rock.

Moreover, under the combined action of shear and normal stresses, a certain degree of counterclockwise rotation occurred in the grouting reinforcement area (Fig. 9(b)), which is reflected in Fig. 9(a) as the displacement concentration in the *Y*-direction on both sides of the grouting area. This phenomenon indicates

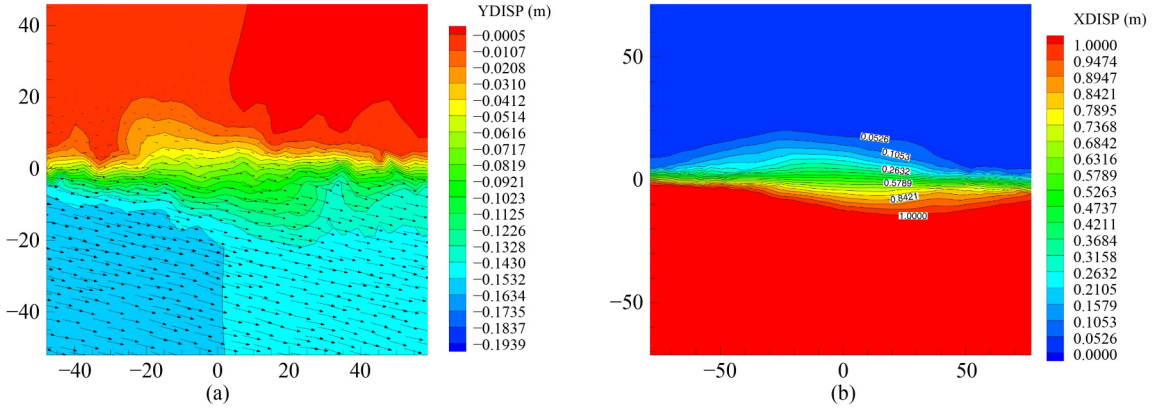

Fig. 7 Displacement contour and displacement vector of the rock mass in the *X* and *Y* directions with local anchor cable modification: (a) displacement vector and *Y*-displacement (YDISP) contour; (b) contour of *X*-direction (XDISP) displacement.

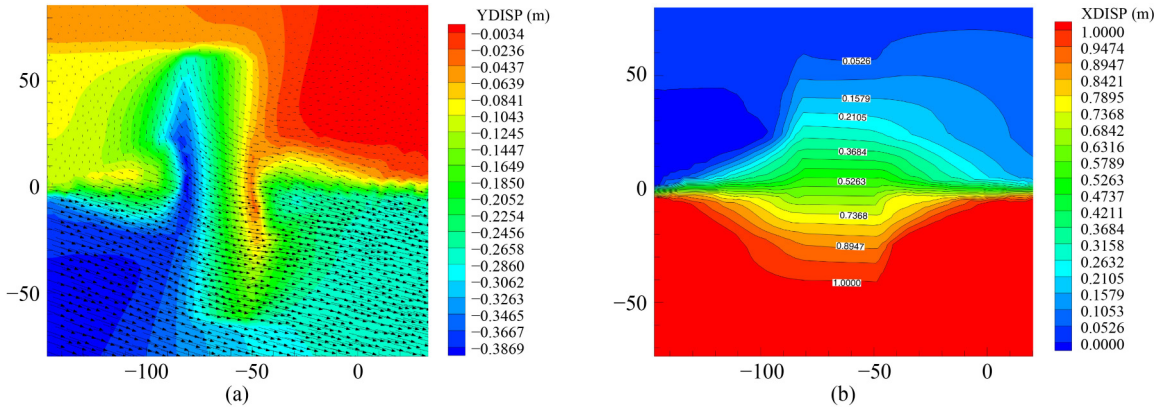

Fig. 8 Displacement contour and displacement vector of the rock mass in the *X* and *Y* directions with local reinforcement of the anti-fault cavern: (a) displacement vector and *Y*-displacement contour; (b) contour of *X*-direction displacement.

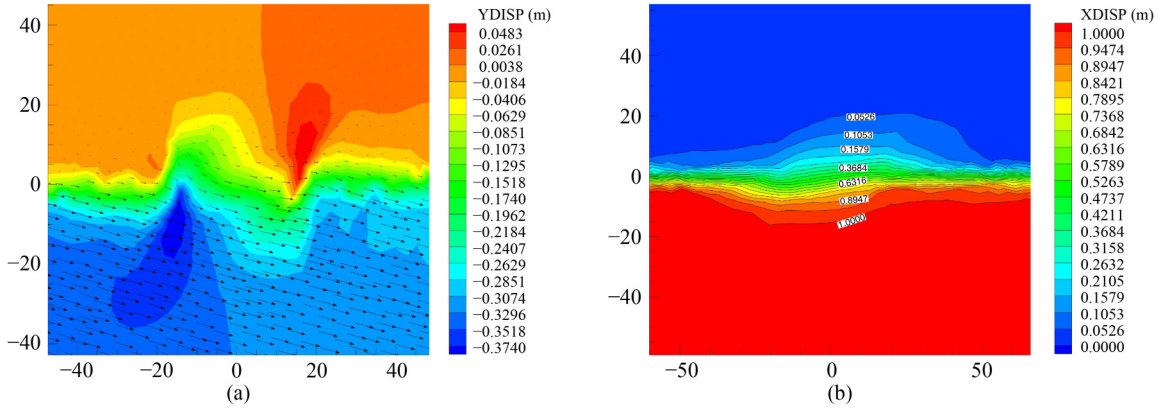

Fig. 9 Displacement contour and displacement vector of the rock mass in the *X* and *Y* directions with local rock mass grouting modification: (a) displacement vector and *Y*-displacement contour; (b) contour of *X*-direction displacement.

that the grouting reinforcement measure improved the bonding ability of the hanging wall and footwall rock mass in the modified grouting area. Moreover, the anti-fault cavern resists dislocation displacement of the two plates of the rock mass in the dislocation zone. This dispersed the concentrated dislocation displacement into two plates of a stable surrounding rock mass.

Notably, the anti-fault effect of the three LRAF methods on the strike-slip active faults with distributed displacement patterns was better than that of the concentrated displacement mode. This occurs because the existence of fault effects provides a transition for the stiffness difference between the stable surrounding rock and fault-affected zone. LRAF methods transfer the concentrated dislocation displacement to the stable surrounding rock more easily, and the reduction in the displacement gradient is more pronounced in the fault dislocation zone.

3.2 Influence on the stress field of the surrounding rock

Furthermore, the four contours of the surrounding rock mass in the distributed strike-slip active fault used three LRAF measures with the control group as an example (where the sign of the principal stress is that the tensile stress is positive, and the compressive stress is negative). The maximum principal stress field (Fig. 10) shows that the LRAF measures significantly influence the stress field of the rock surrounding the fault.

As shown in Fig. 10(a), when no LRAF method exists in the surrounding rock, the stress field of the rock mass near the fault-affected zone and fracture zone is primarily a compressive shear composite. In addition, during the continuous dislocation of the fault, the rock mass of the fault fracture zone and the fault-affected zone are transformed into a plastic state and lose their support ability, which complicates tunnel-support work.

As shown in Fig. 10(b), when an anchor cable is adopted, the continuous dislocation movement of the fault rock mass drives both ends of the anchorage area to stretch the anchorage ends of the anchor cable. The anchor cable produces a resistance force during stretching, which reacts with the rock mass and causes tensile displacement. Therefore, a tensile stress zone appeared near the anchorage ends of the anchor cable, which was also the main reason for the *Y*-direction displacement in the cable-modified area (Fig. 7(a)). The rock mass around the no-grouting section of the anchor

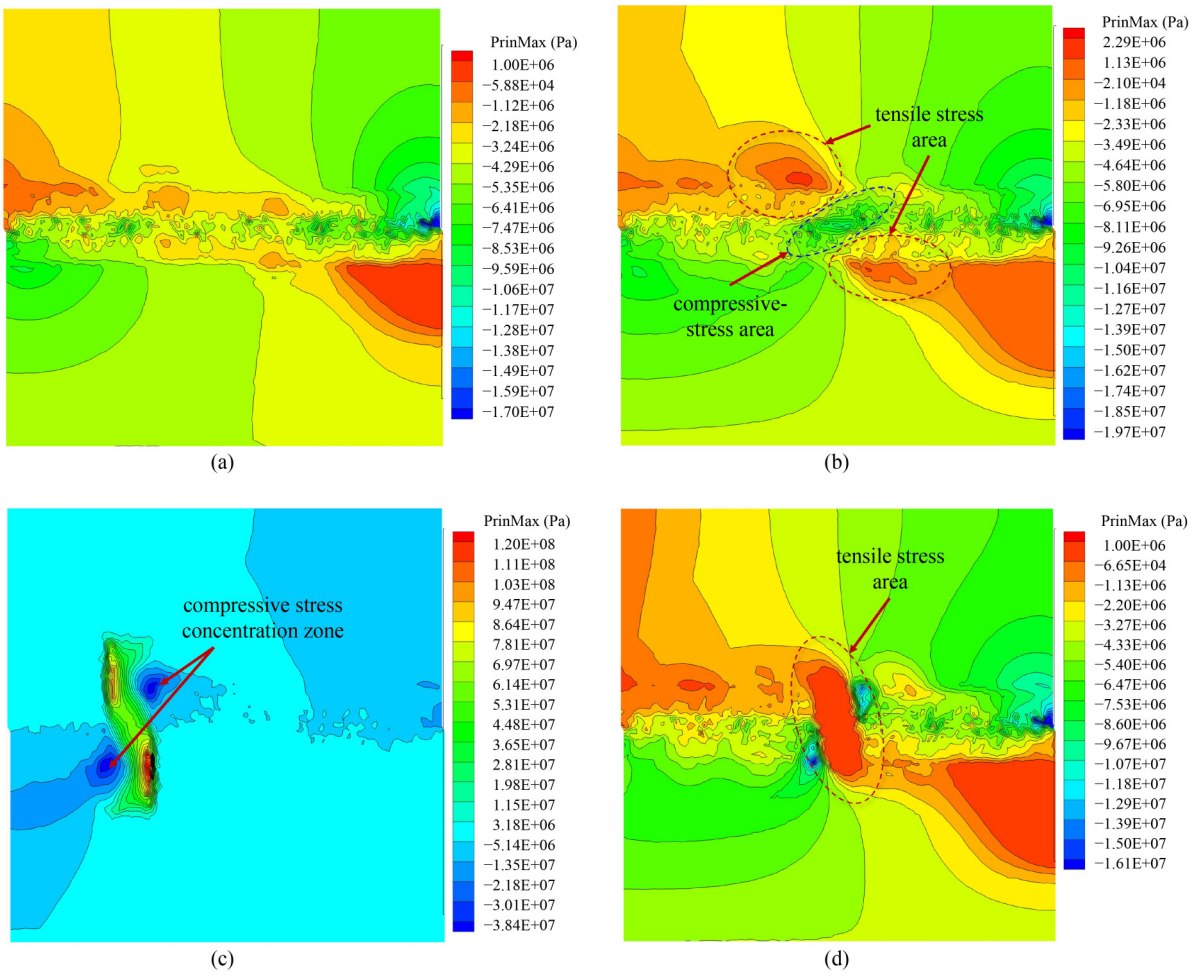

Fig. 10 Stress field of the surrounding rock under different LRAF measures: (a) none of the LRAF measures; (b) anchor cable; (c) anti-fault cavern; (d) local rock mass grouting modification.

cable changes under the action of the reaction force of the anchor cable, and the absolute value of the maximum principal stress and the intermediate principal stress increases (Fig. 11), thus improving the support ability of the rock mass in this area. This area is known as the artificial safety island. When the tunnel passes through the strike-slip active fault from the artificial safety island, the support state of the surrounding rock is good, and the displacement gradient clearly decreases, which is beneficial to the tunnel's support work.

As shown in Fig. 10(c), when the anti-fault cavern was adopted, the anti-fault cavern structure deformed under the shear action produced by fault dislocation. Moreover, two compressive-stress concentration areas formed in the rock mass on both sides of the anti-fault cavern. This is because the stiffness of the anti-fault cavern structure is much larger than that of the rock mass, resulting in a reaction force with a large amplitude that prevents fault dislocation displacement. Moreover, the presence of an anti-fault cavern improves the supporting capacity of the surrounding rock mass by increasing maximum principal stress. When the tunnel passes the fault near the anti-fault

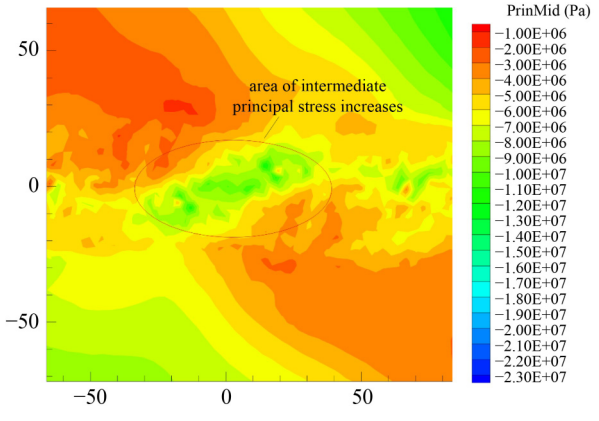

Fig. 11 Increased area of intermediate principal stress in the LRAF zone using anchor cable.

cavern, the difficulty of anti-fault in the tunnel is significantly reduced. Simultaneously, under the shearing force action of the fault, the shear-stress concentration area is formed in the anti-fault cavern (Fig. 12). Therefore, when designing an anti-fault cavern structure,

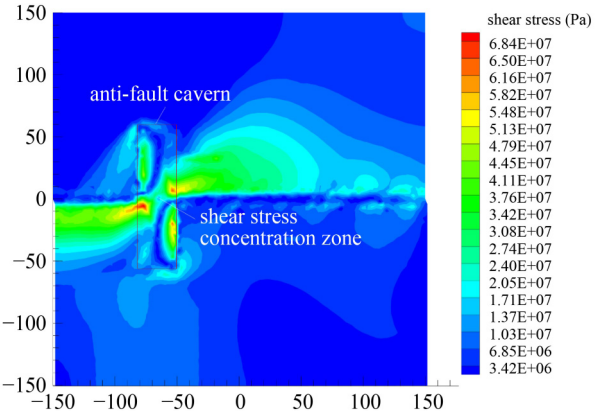

Fig. 12 Shear stress distribution in the rock mass and anti-fault cavern area.

the maximum shear stress in the rock mass should be considered in the material design.

As shown in Fig. 10(d), when the local rock mass grouting modification was adopted, the maximum principal stress field of the surrounding rock was similar to that when using the anti-fault cavern. Moreover, two areas of apparent compressive stress concentration appeared on both sides of the modified grouting area. Therefore, the grouting-modified rock also has a barrier effect on the dislocation displacement. However, the stiffness and strength of the rock mass modified by grouting are far less than those of the anti-fault cavern. Thus, the movement trend of tension appears with the dislocation of the footwall rock mass being pulled. Therefore, the local modification area was a tensile stress area. The dislocation displacement in the *X*-direction of the modification area is transformed into the *Y*-direction displacement (Fig. 9(a)), which reduces the displacement gradient of the tunnel-crossing area. However, the displacement and deformation of the tunnel axis also increased. Therefore, when local grouting modification measures are adopted, the tunnel should take measures to control the deformation along the tunnel axis.

3.3 Evaluation of the local rock mass-anti-fault effect

Furthermore, the displacement gradient and shear plastic strain were used as indices to evaluate the effects of the LRAF method. Based on the analysis of the *X*-direction displacement of the internal monitoring points of the rock mass under different LRAF methods and Eq. (1), the tunnel displacement gradient across the fault range can be obtained using different LRAF methods.

$$\nabla u = \frac{|u_{i+1} - u_i|}{\Delta d_p}, \tag{1}$$

where ∇u is the displacement gradient (cm/m), u_i is the displacement for a monitoring point (m), u_{i+1} is the displacement of the next adjacent monitoring point selected u_i (m), and Δd_p is the distance between adjacent monitoring points (m).

Figure 13 shows that the three LRAF methods significantly decrease the rock mass displacement gradient around the tunnel crossing the strike-slip direction compared with those without LRAF methods. When there is no measure, anti-fault cavern, and local grouting modification, the displacement gradient curve is similar in shape and only changes at the peak. When the local rock mass modification of the anchor cable is adopted, the width of the middle peak part of the displacement gradient curve increases compared with that of the other three curves. The peak width equals the sum of the fault fracture zone width and the fault-affected zone width. Therefore, it is shown that the LRAF method of the anchor cable achieves the anti-fault effect by dispersing the concentrated large deformation into the small to minuscule-range deformation. In addition, the other two LRAF methods carry fault resistance through blocking dislocation displacement, which is consistent with the law shown in Fig. 6. The displacement gradient of the local rock mass grouting modification is the lowest, followed by the anchor cable and anti-fault cavern.

For concentrated strike-slip active faults, the principle of LRAF is the same as that of the distributed fault

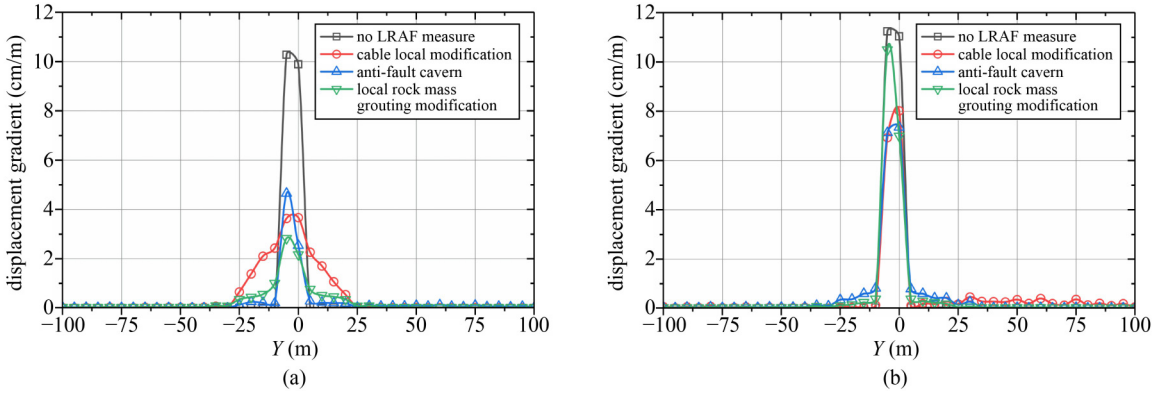

Fig. 13 Displacement gradient curves with different LRAF measures: (a) distributed strike-slip faults; (b) concentrated strike-slip fault.

resistance. However, Fig. 13(b) shows that the anti-fault effect was slightly worse than that of the distributed faults. The displacement gradient curve of the anchor cable under the concentrated fault differed from that under the distributed fault, and the middle peak part of the curve did not significantly expand. The main reason is that the strength of the surrounding rock on both sides of the fracture zone is high, and its ability to provide dispersion displacement is weak. Moreover, there is no corresponding weak fault-affected zone on either side of the fault fracture zone, which can quickly disperse displacement.

However, under concentrated strike-slip faults, three LRAF methods still work, among which the anti-fault effect of the anti-fault cavern is the best, followed by the anchor cable and grouting modification. As the dislocation displacement of a concentrated strike-slip fault is more concentrated than that of a distributed fault, the effect of rigid displacement isolation can have a more significant advantage under this condition. When using local grouting modification, the grouting area is limited to the fracture zone and the modification range is small; thus, the anti-fault effect is poor.

Figure 14 shows the variation in the peak displacement gradient with dislocation displacement of the footwall rock mass. For the distributed strike-slip active fault (Fig. 14(a)), the displacement gradient increases linearly with no LRAF measure and with the LRAF methods of anchor cable and anti-fault cavern measures. However, the increase in the displacement gradient is nonlinear with the LRAF method of local rock mass grouting modification, and the slope increases gradually with the addition of dislocation displacement. The modified area underwent gradual shear failure because of the increased dislocation displacement. The anti-faulting ability of the grouting rock mass area gradually decreased, and the slope of the displacement gradient curve increased with the strike-slip displacement.

For the concentrated strike-slip fault (Fig. 15(b)), in addition to the displacement curve of the local rock mass grouting modification, a nonlinear phenomenon also appears at the beginning of the curve when the anti-fault cavern is adopted. Owing to the concentrated dislocation, the anti-fault cavern produces considerable resistance to the dislocation of the surrounding rock, and the stiffness of the anti-fault cavern is greater than that of the rock mass. Therefore, the rock mass around the anti-fault cavern was squeezed, causing a certain degree of plastic failure. Moreover, the plastic failure only affects some areas adjacent to the anti-fault cavern, and the curve then returns to linear growth after a certain dislocation displacement.

In addition, the equivalent shear plastic strain was used to evaluate the anti-fault effects of the three LRAF methods. Figure 15 shows the contour of the equivalent shear plastic strain, which is compared under different LRAF methods, as shown in Fig. 16.

Figures 15 and 16 show that for strike-slip faults under distributed and concentrated faults, the shear plastic strain is the lowest when local anchor cable modification is adopted, and the anti-fault effect is the best. The shear plastic strain decreases by 64.7% and 46.9%, respectively. Moreover, local grouting modification has a better anti-fault effect on distributed strike-slip faults, but the concentrated anti-fault effect is weak. The anti-fault effect of the anti-fault cavern on both the distributed and concentrated displacement modes is similar, with a decrease of approximately 20%.

In conclusion, the anti-fault effect of the anchor cable in the three advanced engineering methods is better than that in the other two methods, and the mechanical properties of the anchor cable are more suitable for tunnel anti-fault engineering. The anti-fault cavern and local rock mass grouting modifications have a better anti-fault effect on specific fault displacement modes (e.g., concentrated strike-slip active faults). Therefore, it will play a better role in multiple-LRAF joint measurements in a particular geological environment.

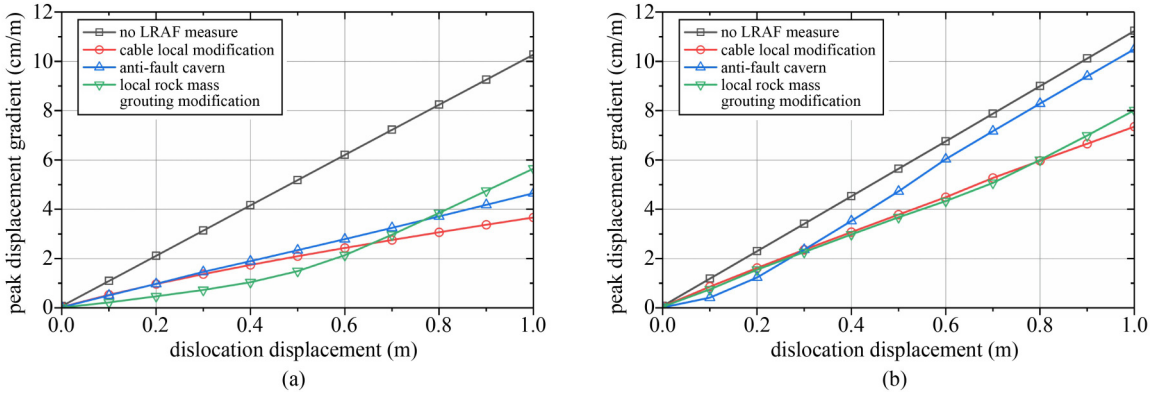

Fig. 14 Variation curve of the displacement gradient with the fault dislocation magnitude: (a) distributed strike-slip faults; (b) concentrated strike-slip fault.

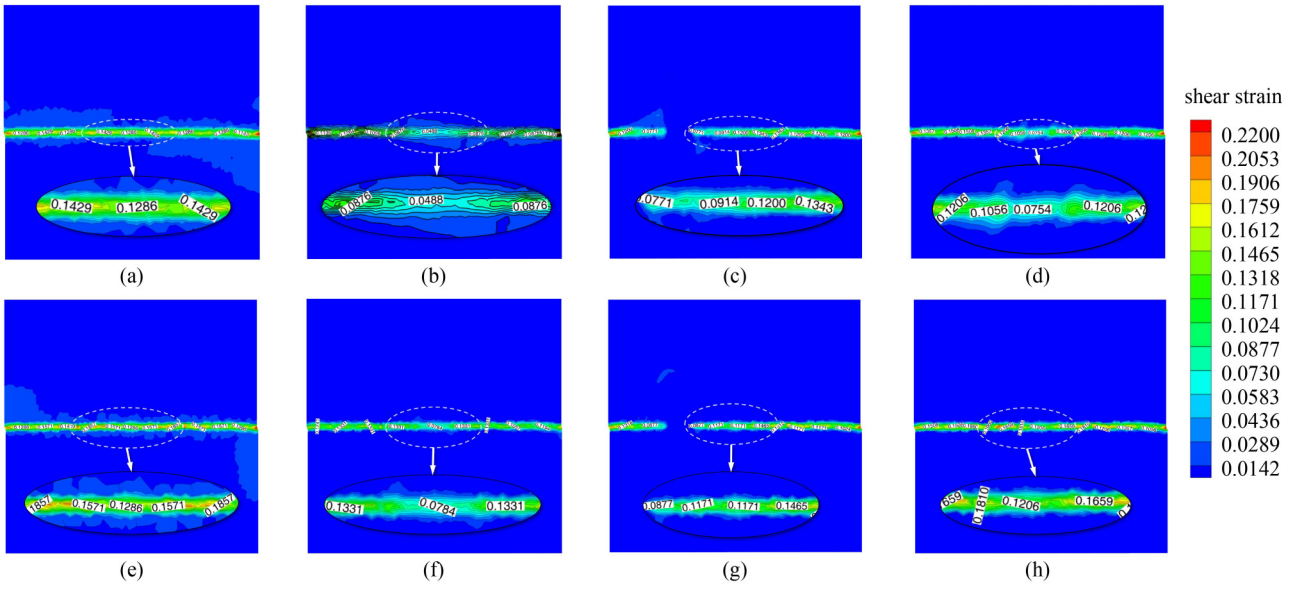

Fig. 15 Equivalent shear plastic displacement of distributed and concentrated strike-slip active fault fracture zones under different LRAF methods: (a) distributed fault without LRAF methods; (b) distributed fault using local anchor cable modification; (c) distributed fault using an anti-fault cavern; (d) distributed fault using local rock mass grouting modification; (e) concentrated fault without LRAF methods; (f) concentrated fault using local anchor cable modification; (g) concentrated fault using an anti-fault cavern; (h) concentrated fault using local rock mass grouting modification;

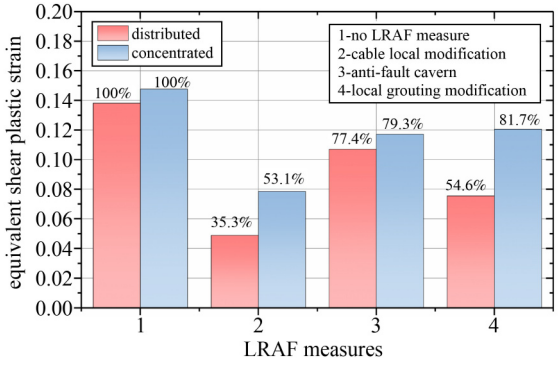

Fig. 16 Summary of the shear plastic strain of the strike-slip active fault zone under different LRAF methods.

4 Numerical analysis of multiple-joint local rock mass-anti-fault methods

4.1 Influence on the displacement field of the surrounding rock and stress law of the anchor cable

According to the abovementioned research, the anti-fault effect of a single LRAF method has not yet achieved ideal results for faults with concentrated dislocations and significant dislocation velocities. Therefore, combining anchor cables with one or more measures of the anti-fault cavern or local rock mass grouting modification may achieve better results. The model in Figs. 3(i)–3(p) is used to study the influence of multiple-joint LRAF methods on the displacement field.

After the calculation, Fig. 17 shows the *X*-direction displacement nephogram and *X*-direction displacement curve of the tunnel axis. The anti-fault effect of multiple-joint LRAF methods on dislocation displacement was better than that of a single LRAF method, and the reduction in the displacement gradient in the fault zone was more pronounced.

Figures 17(b) and 17(f) show that the multiple-joint LRAF methods of the anchor cable and anti-fault cavern have a better effect than the single LRAF method, especially for concentrated strike-slip faults. The anti-fault cavern acts as a rigid barrier to fault displacement, and the displacement gradient of the surrounding rock near the anti-fault cavern has already decreased before the anchor cables exist. When an anchor cable is adopted for joint LRAF methods, the decrease in the displacement gradient is more significant because of the recovery of the specific support capacity of the surrounding rock. The displacement vector diagram shows that the anti-fault cavern contains a partial barrier displacement from the *X*-direction displacement transformed into *Y*-direction displacement. The displacement in the *Y*-direction of the tunnel-crossing area was further reduced compared to that using the single LRAF method.

In addition, the shape of the *X*-direction displacement curve (Fig. 17) changes compared with that using the single LRAF method, and the effect range and degree of displacement in the surrounding rock are significantly expanded. Figures 17(c) and 17(g) show that the strength of the rock mass in the grouting area was improved through the LRAF method by combining the anchor cable and local grouting modification. Therefore, the diffusion degree of the dislocation displacement is significantly

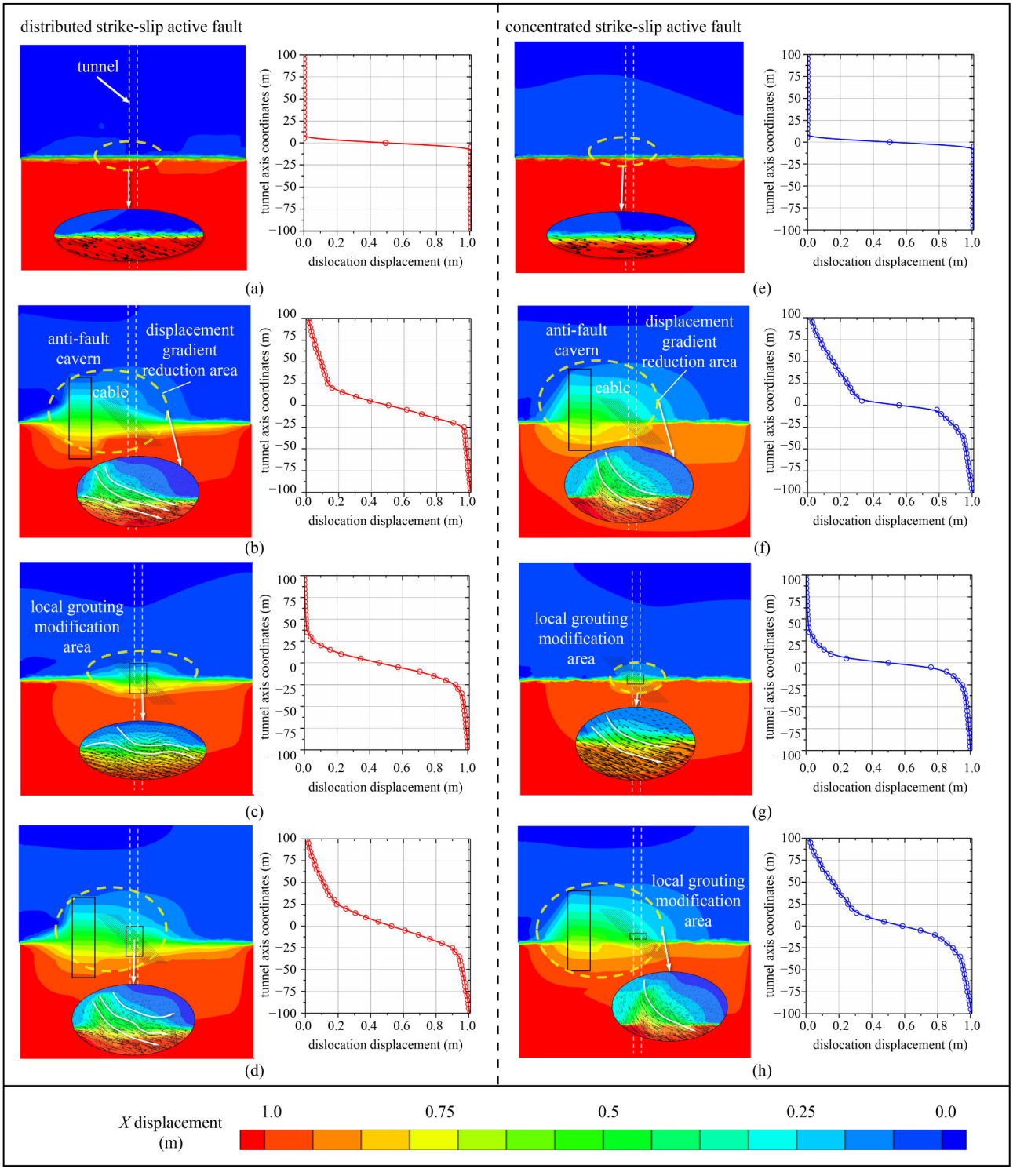

Fig. 17 *X*-direction displacement magnitude and resultant displacement vector of different multiple-joint LRAF methods for distributed and concentrated pattern faults: (a) control group (distributed); (b) anchor cable and anti-fault cavern (distributed); (c) anchor cable and local grouting modification (distributed); (d) three measures combination (distributed); (e) control group (concentrated); (f) anchor cable and anti-fault cavern (concentrated); (g) anchor cable and local grouting modification (concentrated); (h) three measures combination (concentrated).

enhanced compared with a single anchor cable or grouting modification (Figs. 6(b), 6(d), 6(f), and 6(h)). Figures 17(d) and 17(h) show that when the three-joint LRAF methods work in the surrounding rock simultaneously, the displacement diffusion range expands compared to the first two combined control methods, and the slope change of the displacement curve is more pronounced.

Among the aforementioned three-joint LRAF methods, the anchor cable is a key anti-fault for the tunnel. Therefore, the stress resistance of the anchor cable is also the focus of joint LRAF methods. Figure 18 shows that as the dislocation displacement increased, the equivalent tensile force of the anchor cable continuously increased after pretension application. Furthermore, the equivalent tensile force of the anchor cable reached its peak when the footwall rock mass reached a predetermined dislocation displacement. In addition, the equivalent peak tension force of the anchor cable obtained using the joint LRAF method was lower than that obtained using the single LRAF method. Therefore, when the joint LRAF method is adopted, the surrounding rock shares part of the fault displacement and reduces the equivalent peak tension of the anchor cable, thereby providing conditions for applying LRAF methods in engineering.

Under a distributed strike-slip fault, when the joint LRAF methods of the anchor cable and local grouting modification are adopted, the bearing capacity of the grouting area is continuously reduced under continuous dislocation. Furthermore, the fault dislocation resistance gradually transitions to that of an anchor cable with a weakened anti-fault effect of the modified area on the fault. Hence, the tension-force curve of the anchor cable is nonlinear. Under the concentrated strike-slip fault, the reinforcement zone area was small and the anti-fault effect on the fault was poor. Therefore, the anchor cable operates in the anti-fault process, and its tension force increases linearly. Moreover, for the multiple-joint LRAF methods of the double displacement patterns, the tension force of the anchor cable is the smallest when the three-joint LRAF methods are adopted; thus, it is the optimal choice when the tensile strength of the anchor cable is limited.

4.2 Anti-fault effect evaluation of multiple-joint local rock mass-anti-fault methods

Figure 19 shows that the slope of the displacement curve's middle section significantly decreases when the multiple-joint LRAF methods are adopted. Figures 19(a) and 19(b) show that the displacement gradient presents an increasing linear trend with the dislocation displacement. When grouting modification is added to multiple-joint LRAF methods, the damage degree of the modified area gradually increases with dislocation displacement. The fault resistance is weakened, and the displacement gradient increases nonlinearly.

Furthermore, the multiple-joint LRAF methods achieved an excellent anti-fault effect for distributed strike-slip faults (Fig. 19(c)). Among them, the displacement gradient of the three advanced engineering measures in the joint LRAF methods was the lowest. At the same time, the other two combinations of multiple-joint LRAF methods have the same effect. For the concentrated strike-slip fault (Fig. 19(d)), the degree of decline of the displacement gradient and the degree of displacement diffusion using the combination of the two methods for multiple-joint LRAF methods were better than those using a single method. The use of the three-joint-anti-fault measures can still achieve a better effect.

Notably, under the concentrated strike-slip active fault, the multiple-joint LRAF methods have a better dispersion effect on the concentrated dislocation displacement. The displacement curve (Fig. 19) shows that the diffusion range of concentrated dislocations is often limited to the fault fracture zone and fault-affected zone when using a single LRAF method. Moreover, the displacement diffusion range can be extended to a stable surrounding rock when using multiple-joint LRAF methods. Therefore, it plays the LRAF role of a stable rock mass better, creating better supporting conditions for the tunnel.

At the same time, Fig. 20 shows the contour of the equivalent shear plastic strain, and Fig. 21 evaluates the anti-fault effect of different multiple-joint LRAF methods. Under the distributed fault, Fig. 20 shows that the equivalent shear plastic strain is the lowest when the anchor cable and anti-fault cavern are used for the multiple-joint LRAF method. Because the anti-fault cavern blocked most of the dislocation displacement,

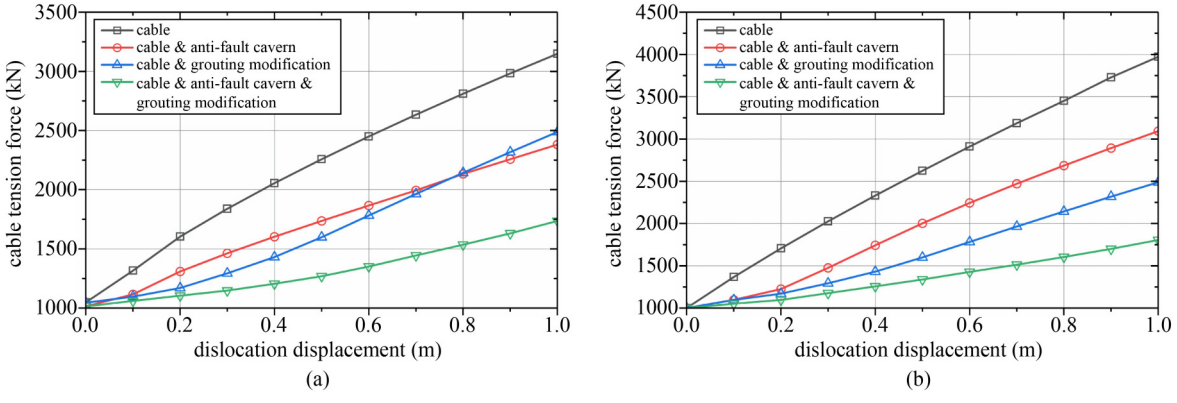

Fig. 18 Relationship between the tension force of the anchor cable and the dislocation magnitude: (a) distributed; (b) concentrated.

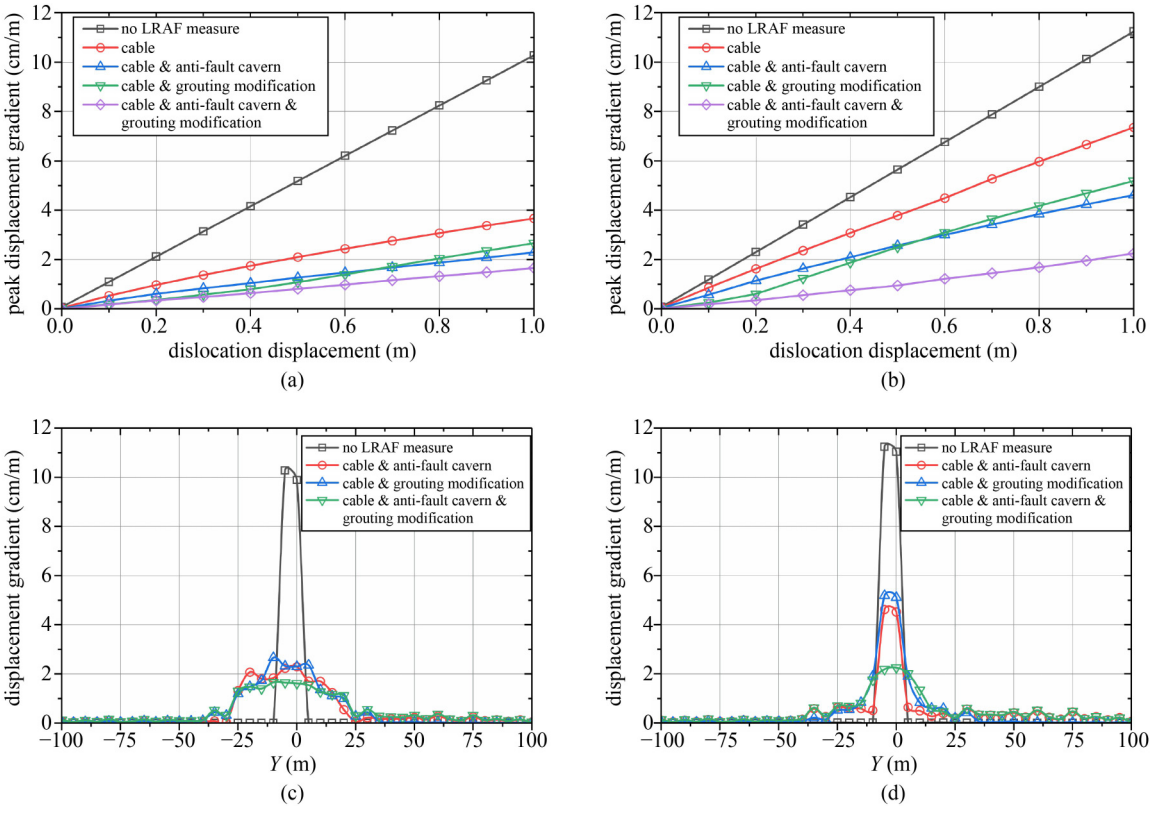

Fig. 19 Curves of the displacement gradient versus dislocation displacement and displacement gradient at each monitoring point with a dislocation magnitude of 1.0 m: (a) distributed fault peak displacement gradient; (b) concentrated fault peak displacement gradient; (c) distributed fault displacement gradient; (d) concentrated fault displacement gradient.

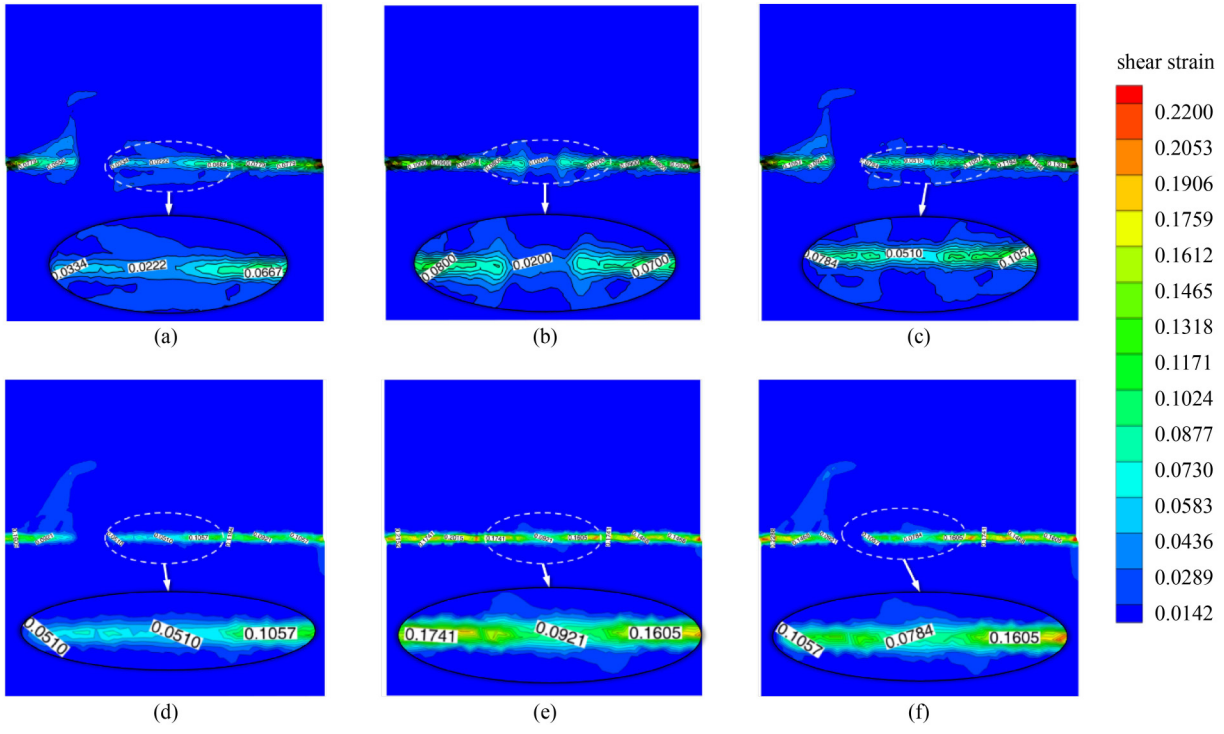

Fig. 20 Contour of the equivalent plastic strain of the surrounding rock under multiple-joint LRAF methods: (a) anchor cable and anti-fault cavern (distributed); (b) anchor cable and local rock mass modification (distributed); (c) anchor cable, anti-fault cavern, and local rock mass modification (distributed); (d) anchor cable and anti-fault cavern (concentrated); (e) anchor cable and local rock mass modification (concentrated); (f) anchor cable, anti-fault cavern, and local rock mass modification (concentrated).

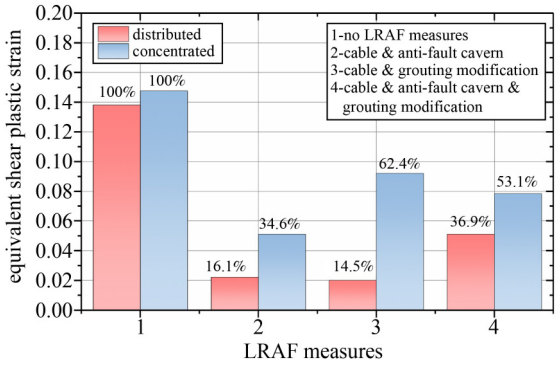

Fig. 21 Summary of equivalent shear strain under different multiple-joint LRAF methods.

continued use of the anchor cable for LRAF can achieve satisfactory results. Figures 20(c) and 20(f) show that when the three methods were adopted for the joint LRAF methods, the equivalent shear plastic strain increased slightly. Because the dislocation displacement of the tunnel position has been reduced to a low magnitude under the action of the anti-fault cavern and local rock mass modification, in this case, the tensile elongation of the anchor cable is reduced because the resistance force value is low. The anti-fault role of the anchor cable was small, and the dispersion of the fault displacement was reduced accordingly. Therefore, the shear plastic strain rebounded.

In summary, the anti-fault effects of the multiple-joint LRAF methods were evaluated. When three advanced engineering measures of joint LRAF methods are adopted, the displacement gradient is the smallest, and the anchor cable tension force is the smallest. Furthermore, the joint LRAF method for anchor cables with a single anti-fault cavern or local rock mass grouting modification are the best under distributed strike-slip active faults. Under concentrated strike-slip faults, anti-fault caverns can play a more significant role. Its combination with anchor cables in the LRAF method can achieve a better effect. Therefore, the selection of the LRAF method in engineering must consider many factors and determine the LRAF scheme.

5 Verification of anchor cable local modification under the three-dimensional model

Based on the methodology and results of the two-dimensional calculation, the effect of the anchor cable on the displacement and stress fields of the surrounding rock was verified. A three-dimensional numerical model was established according to the two-dimensional numerical model, and the mesh of the anchor cable modification area was mesh densified. In total, 550000 tetrahedral elements were generated in the model, as shown in Fig. 22. Subsequently, the methodology and boundary conditions of the two-dimensional LRAF simulation were adopted, and the maximum dislocation displacement was set to 1 m. After the calculation, the following results were obtained.

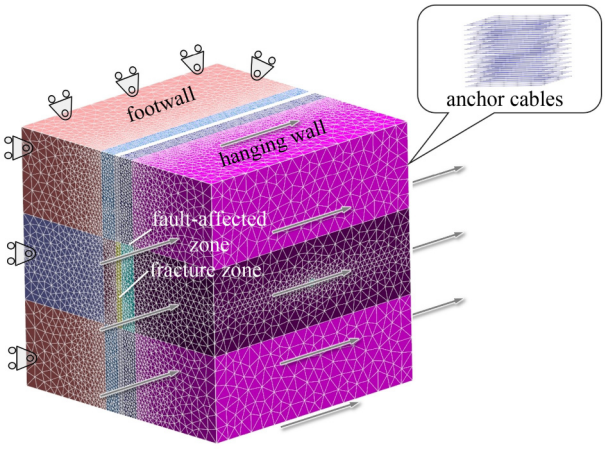

Fig. 22 Three-dimensional numerical model of the anchor cable LRAF method.

The simulation results were analyzed by selecting the cross-sections of the *X*- and *Z*-direction at the center of the model. Figure 23 shows that the local modification area of the anchor cable significantly reduces the displacement gradient in both the *Y*- and *Z*-direction compared with the two-dimensional calculation. Moreover, the peak displacement gradient of the tunnel-crossing position is 3.55 cm/m, which was 53.10% lower than that without the LRAF method. The maximum principal stress nephogram in Fig. 24 shows the same law as the two-dimensional calculation results (Fig. 10(b)), which verifies the reliability of the two-dimensional calculation.

Figure 23 shows that the displacement gradient in the *Y*- and *Z*-direction decreases in the modified area of the anchor cable. Therefore, there is a region where the concentrated dislocation displacement is significantly diffused in the modified area. The displacement gradient of the tunnel passing through the region is lower than that directly passing through the active fault zone, called the artificial safety island. The iso-surfaces with displacements of 0 and 1 m are extracted, and the three-dimensional model of the artificial safety island area is drawn, as shown in Fig. 25. This shows that the artificial safety island area has an ellipsoid shape. The area size is equal to the local modification area of the anchor cable. The displacement gradient decreases when the tunnel passes through the artificial safety island area. The surrounding rock outside the area maintains the maximum dislocation magnitude, which verifies the theoretical feasibility of the LRAF methods.

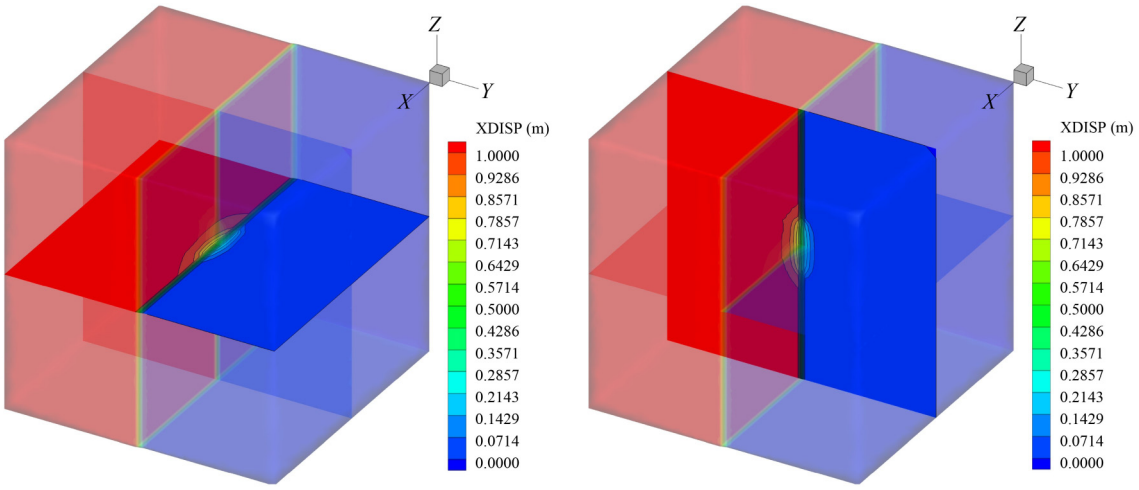

Fig. 23 *X*-direction displacement contours of the *X*- and *Z*-direction sections in three-dimensional numerical model.

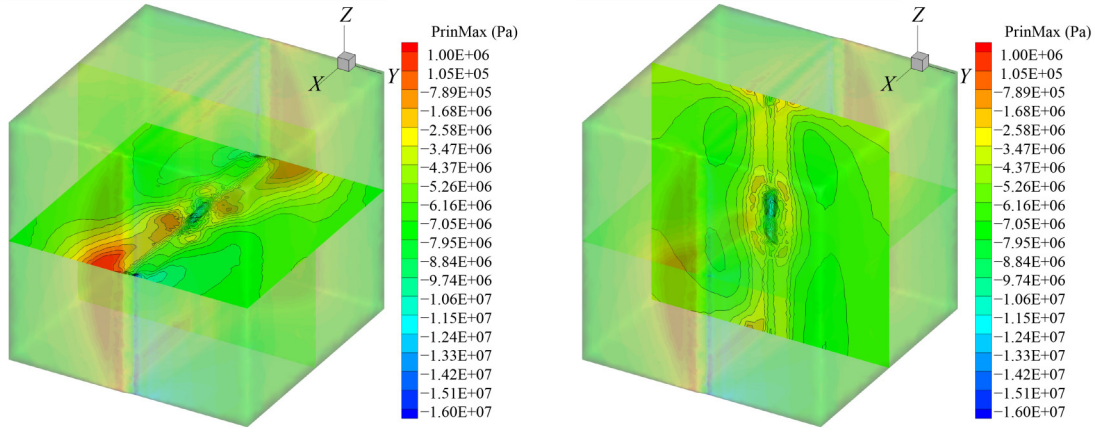

Fig. 24 Maximum principal stress contours of the *X*- and *Z*-direction sections in three-dimensional numerical model.

6 Discussion

It should be noted that the influence of single- or multiple-LRAF methods on the displacement and stress fields of the surrounding rock has specific characteristics. This study provides theoretical guidance for the application of the LRAF method in engineering. From this study, the core idea of the LRAF method is obtained, allowing fault displacement, using single or multiple advanced engineering measures to disperse the concentrated large dislocation deformation into tiny local deformations, and reducing the fault displacement gradient. The anti-fault ability of the existing latest support technology is fully exerted, and the surrounding rock is used as a container for displacement transfer, which guarantees the anti-fault support of tunnels crossing strike-slip faults.

Through this research, it can be noted that the core of single- and multiple-joint LRAF methods is the anchor cable. It changes the stress and strain fields of the surrounding rock in the modified area through its mechanical characteristics, improves the support ability of the rock mass, and reduces the difficulty of tunnel support. Moreover, the concentrated fault dislocation is dispersed in the fault-affected zone and the stable surrounding rock owing to its prominent deformation characteristics. This minimized the displacement gradient of the tunnel crossing the fault. Figure 18 shows that the equivalent tensile force is the largest when the anchor cable is adopted alone for the LRAF method, reaching 3000 and 4000 kN (300 and 400 t, respectively) under the conditions of distributed and concentrated strike-slip active faults. The maximum constant resistance force of the NPR anchor cable can reach 850 kN; thus, arranging three or four anchor cables in the same position is necessary to realize the LRAF effect. When multiple-LRAF methods are adopted jointly, the required constant resistance of the anchor cable decreases. Therefore, the same anti-fault effect can be achieved by arranging a smaller number of NPR anchor cables, which creates the possibility of the engineering realization of LRAF methods.

In addition, Fig. 26 shows the peak displacement

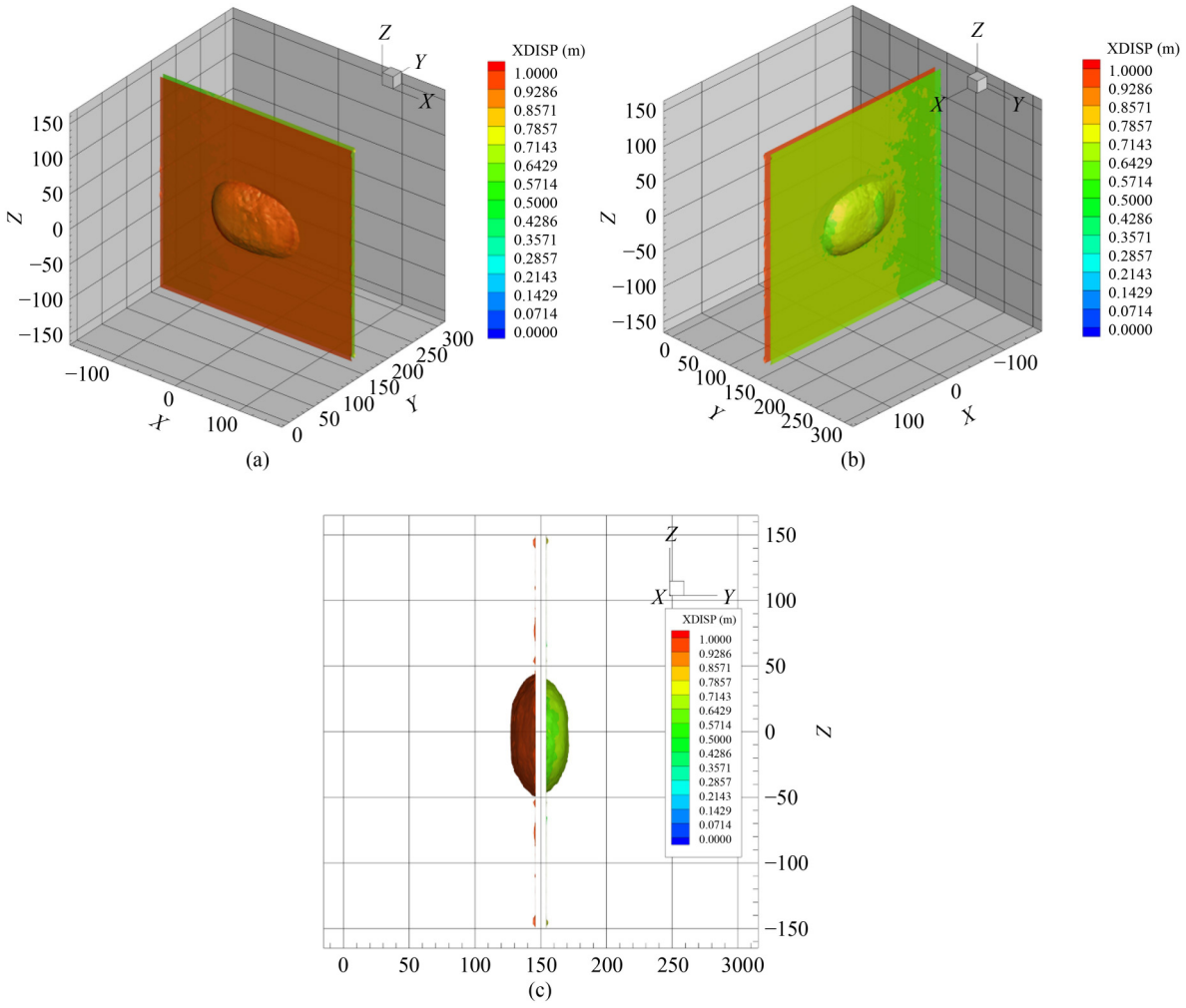

Fig. 25 Artificial safety island model: (a) three-dimensional model of an artificial safety island in the *Y*-positive direction; (b) three-dimensional model of an artificial safety island in the *Y*-negative direction; (c) three-dimensional model of an artificial safety island.

gradient and equivalent shear plastic strain using the single- and multiple-joint LRAF methods. When the fault creep rate is not too high for distributed strike-slip faults, local anchor cable modification, local rock mass grouting modification, or two-joint LRAF measures can achieve a better anti-fault effect. Moreover, the engineering costs of the two LRAF methods are low and easy to realize. When the fault creep rate is high, the anti-fault cavern should be set to prevent dislocation displacement and the anchor cable should be combined to achieve a better anti-fault effect. When the fault rate is high and the constant peak resistance force of the anchor cable is insufficient, the multiple-joint LRAF method of the three advanced engineering measures should be considered. However, the construction cost and implementation of the multiple-joint LRAF method of three advanced engineering measures are challenging; thus, it should be considered when the fault conditions are highly unfavorable. In the case of distributed strike-slip active faults, two-joint LRAF methods are better in terms of supporting effect and cost, which should be prioritized.

An anti-fault cavern can play a better role under a concentrated fault. Therefore, the anti-fault cavern should be preferentially set and combined with the anchor cable in the LRAF method to achieve a better anti-fault effect. When the fault condition is unfavorable to the support, the multiple-joint LRAF method of three advanced engineering measures is preferred to reduce the displacement gradient.

In addition, the influence of LRAF measures on the tunnel structure is a critical issue that needs to be considered. According to relevant research, a change in the fault dislocation magnitude will change the tunnel displacement mode, resulting in different failure forms of the tunnel-supporting structure, and the failure position usually appears at a position with a large displacement gradient [1,57,58]. According to previous research results, different LRAF measures will have different effects on the tunnel displacement pattern, particularly as shown by the shape of the S-shaped displacement curve on the tunnel axis. For example, when the local modification of the anchor cable is adopted (Figs. 6(b)

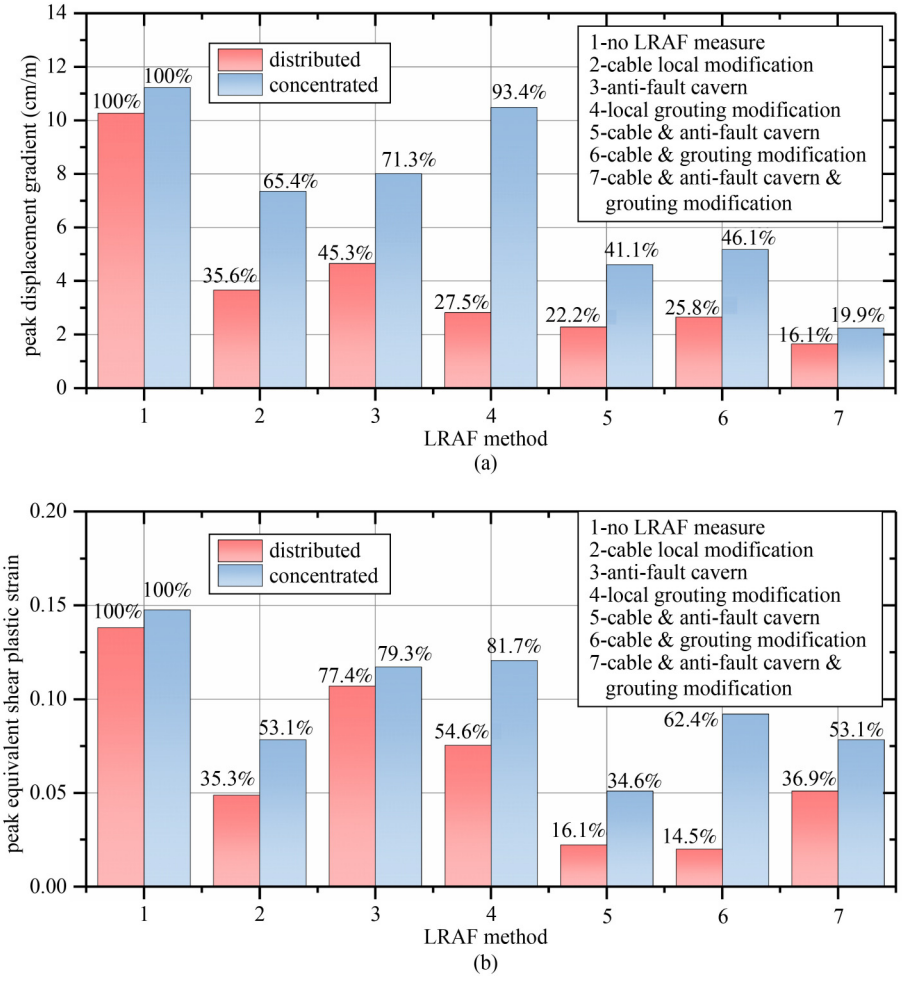

Fig. 26 Summary of peak displacement gradient and peak equivalent shear plastic strain under single and multiple-LRAF methods: (a) peak displacement gradient; (b) peak equivalent shear plastic strain.

and 6(e)), the concentrated dislocation displacement is dispersed in the local modification area of the anchor cable. Thus, the peak displacement gradient decreases, but the range of the displacement gradient increases. When an anti-fault cavern is adopted (Figs. 6(c) and 6(g)), the anti-fault cavern structure transfers the concentrated dislocation displacement to the stable rock mass of the hanging wall rock mass; thus, the peak displacement gradient decreases, but the dislocation displacement of the rock mass in the hanging wall rock mass increases. Therefore, different tunnel-supporting structures must be redesigned according to different LRAF measures, and this constitutes new research topic.

7 Conclusions

Based on single or multiple-joint forms of three advanced engineering measures—local anchor cable modification, local reinforcement of anti-fault, and local rock mass grouting modification—this study proposes an LRAF method for tunnels crossing strike-slip active faults with two displacement patterns. The influence of the LRAF method on the displacement of the surrounding rock and the stress field of the tunnel under two- and three-dimensional conditions was investigated using a numerical method, and the anti-fault effect was evaluated. The following conclusions are drawn.

1) The concept of LRAF methods is to allow dislocation displacement of the rock mass on both sides of the fault. However, in the local area of the tunnel crossing the active fault, single- or multiple-joint measures in the local modification of the anchor cable, local reinforcement of the anti-fault cavern, and local rock mass grouting modification are adopted to disperse the concentrated large dislocation displacement into a small local deformation. Thereafter, corresponding support measures can be taken to protect the tunnel without damaging the dislocation displacement.

2) Three advanced engineering measures significantly changed the displacement field distribution of the surrounding rock in the cross-fault area of the tunnel. Local modification of the anchor cable dispersed the dislocation displacement into the stable surrounding rock

of the hanging wall and the footwall rock mass. It transformed the concentrated large dislocation deformation into a small-gradient dislocation deformation, which reduced the difficulty of supporting the tunnel across the fault position. The anti-fault cavern strongly resisted dislocation displacement through ultrahigh-strength concrete. It absorbed the dislocation deformation using the stiffness difference between the anti-fault cavern and the surrounding rock. This reduced the maximum dislocation magnitude and displacement gradient of the local surrounding rock mass. Local rock mass grouting modification improved the supporting capacity of the fault-fracture and fault-affected zones surrounding the rock, thereby resisting the maximum dislocation magnitude of the modified area to a lower extent and reducing the displacement gradient.

3) Three advanced engineering measures significantly changed the stress-field distribution in the rock surrounding the cross-fault tunnel. The anchor cable converted the tensile stress field of the modified local area into a compressive stress field. This improved the support ability of the surrounding rock in the modified area by increasing the intermediate principal stress. In addition, the anti-fault cavern absorbed the shear stress generated by fault dislocation into the anti-fault cavern structure. This reduced the shear force on the tunnel structure. Moreover, the local rock mass-grouting-modified area improved the supporting capacity of the surrounding rock, thereby increasing the sliding resistance force of the fault in the modified local area. Furthermore, the stress field in the grouting modification area was transformed from shear stress in the fault slip direction to tensile stress in the axial tunnel direction, thereby reducing the displacement gradient.

4) The effects of the multiple-joint LRAF method were evaluated. For distributed strike-slip faults, anchor cables combined with local grouting modifications or anti-fault caverns exhibited better economic and anti-fault effects. For a concentrated strike-slip fault, the anti-fault cavern can play a more significant role, and the anchor cable combined with the anti-fault cavern in the LRAF method can have a superior anti-fault effect.

5) The anchor cable is the core of the LRAF method. A combination of anchor cables and other advanced engineering measures for the LRAF method can form an artificial safety island at the tunnel cross-fault position of the surrounding rock mass. The rock mass in this area has an excellent bearing capacity and low displacement gradient, which provides tunnel protection. In addition, three-dimensional numerical results verified this conclusion.

This study verified the theoretical feasibility of applying LRAF methods for tunnels crossing strike-slip faults. However, further studies are required before this method can be adopted for engineering applications. In future, further experimental and engineering research should be conducted to solve the problems associated with applying the LRAF method in engineering, and to provide innovative ideas for tunnel anti-fault measures.

Acknowledgements This work was supported by the National Natural Science Foundation of China (Grant No. 41941018), Scientific Instrument Developing Project of the Chinese Academy of Sciences (No. YJKYYQ20200040), Key Research Program of Frontier Sciences of the Chinese Academy of Sciences (No. ZDBS-LY-DQC022), and Knowledge Innovation Program of Wuhan-Basic Research (No. 2022010801010160).

Conflict of Interests The authors declare that they have no conflict of interest.

References

1. Zhang C, Liu X, Zhu G, Zhou H, Zhu Y, Wang C. Distribution patterns of rock mass displacement in deeply buried areas induced by active fault creep slip at engineering scale. Journal of Central South University, 2020, 27(10): 2849−2863
2. Aygar E B, Gokceoglu C. A special support design for a large-span tunnel crossing an active fault (T9 Tunnel, Ankara-Sivas High-Speed Railway Project, Turkey). Environmental Earth Sciences, 2021, 80(1): 37
3. Prentice C S, Ponti D J. Coseismic deformation of the Wrights tunnel during the 1906 San Francisco earthquake: A key to understanding 1906 fault slip and 1989 surface ruptures in the southern Santa Cruz Mountains, California. Journal of Geophysical Research, 1997, 102(B1): 635−648
4. Cui G, Wu X, Wang M, Lin G. Highway tunnel damage caused by earthquake and its mechanism crossing fault zone in Wenchuan Earthquake Area. Chinese Journal of Geological Hazard and Control, 2018, 29(2): 108−114
5. Blanchard F B, Laverty G L. Displacements in claremont water tunnel at intersection with Hayward fault. Bulletin of the Seismological Society of America, 1966, 56(2): 291−294
6. Ryan H F, Parsons T, Sliter R W. Vertical tectonic deformation associated with the San Andreas fault zone offshore of San Francisco, California. Tectonophysics, 2008, 457(3−4): 209−223
7. Zoback M L, Jachens R C, Olson J A. Abrupt along-strike change

in tectonic style: San Andreas fault zone, San Francisco Peninsula. Journal of Geophysical Research, 1999, 104(B5): 10719−10742
8. Bilham R, Bodin P. Fault zone connectivity-slip rates on faults in the San Francisco bay area, California. Science, 1992, 258(5080): 281−284
9. Malservisi R, Gans C, Furlong K P. Numerical modeling of strike-slip creeping faults and implications for the Hayward fault, California. Tectonophysics, 2003, 361(1−2): 121−137
10. Xue Y, Kong F, Yang W, Qiu D, Su M, Fu K, Ma X. Main unfavorable geological conditions and engineering geological problems along Sichuan−Tibet railway. Chinese Journal of Rock Mechanics and Engineering, 2020, 39(3): 445−468
11. Dalgıç S. Tunneling in squeezing rock, the Bolu tunnel, Anatolian Motorway, Turkey. Engineering Geology, 2002, 67(1−2): 73−96
12. Lu C, Cai C. Challenges and countermeasures for construction safety during the Sichuan−Tibet railway project. Engineering, 2019, 5(5): 833−838
13. Rehbock-Sander M, Jesel T. Fault induced rock bursts and micro-tremors—Experiences from the Gotthard Base Tunnel. Tunnelling and Underground Space Technology, 2018, 81: 358−366
14. Lin D, Yuan R, Shang Y, Bao W, Wang K, Zhang Z, Li K, He W. Deformation and failure of a tunnel in the restraining bend of a strike-slip fault zone: An example from Hengshan Mountain, Shanxi Province, China. Bulletin of Engineering Geology and the Environment, 2017, 76(1): 263−274
15. Kiani M, Akhlaghi T, Ghalandarzadeh A. Experimental modeling of segmental shallow tunnels in alluvial affected by normal faults. Tunnelling and Underground Space Technology, 2016, 51: 108−119
16. Loukidis D, Bouckovalas G D, Papadimitriou A G. Analysis of fault rupture propagation through uniform soil cover. Soil Dynamics and Earthquake Engineering, 2009, 29(11−12): 1389−1404
17. Sabagh M, Ghalandarzadeh A. Centrifuge experiments for shallow tunnels at active reverse fault intersection. Frontiers of Structural and Civil Engineering, 2020, 14(3): 731−745
18. Ma Y, Sheng Q, Zhang G, Cui Z. A 3D discrete-continuum coupling approach for investigating the deformation and failure mechanism of tunnels across an active fault: A case study of Xianglushan tunnel. Applied Sciences, 2019, 9(11): 2318
19. Rahman M A, Taniyama H. Analysis of a buried pipeline subjected to fault displacement: A DEM and FEM study. Soil Dynamics and Earthquake Engineering, 2015, 71: 49−62
20. Zhou G, Cui Z, Sheng Q, Wu H, Fu X. Study on the deformation and internal force of the tunnel under the displacement pattern of the active fault zone. Journal of Disaster Prevention and Mitigation Engineering, 2021, 41(6): 1323−1349
21. Wang T Q, Geng P, Li P S, Wang Q, Wang L J. Deformation and failure of overburden soil subjected to normal fault dislocation and its impact on tunnel. Engineering Failure Analysis, 2022, 142: 106747
22. Chatzidakis D, Tsompanakis Y, Psarropoulos P N. Numerical investigation of secondary-fault rupture propagation through sandy deposits. Engineering Geology, 2021, 292: 106258
23. Thebian L, Najjar S, Sadek S, Mabsout M. Numerical investigation of dip-slip fault propagation effects on offshore seabed sediments. Engineering Geology, 2018, 237: 149−167
24. Azizkandi A S, Ghavami S, Baziar M H, Hasanaklou S H. Assessment of damages in fault rupture-shallow foundation interaction due to the existence of underground structures. Tunnelling and Underground Space Technology, 2019, 89: 222−237
25. Zhao K, Chen W, Yang D, Zhao W, Wang S, Song W. Mechanical tests and engineering applicability of fibre plastic concrete used in tunnel design in active fault zones. Tunnelling and Underground Space Technology, 2019, 88: 200−208
26. Huang Q, Peng J, Men Y, Li K. Model test study of sectional metro tunnel with flexible joints adapting large deformation of ground fissures. Journal of Rock Mechanics and Engineering, 2010, 29(8): 1546−1554
27. Zeng G, Geng P, Guo X, Li P, Wang Q, Ding T. An anti-fault study of basalt fiber reinforced concrete in tunnels crossing a stick-slip fault. Soil Dynamics and Earthquake Engineering, 2021, 148: 106687
28. Caulfield R, Kieffer D S, Tsztoo D F, Cain B. Seismic design measures for the retrofit of the claremont tunnel. RETC Proceedings California, 2005, 1128–1138
29. Shahidi A R, Vafaeian M. Analysis of longitudinal profile of the tunnels in the active faulted zone and designing the flexible lining (for Koohrang-III tunnel). Tunnelling and Underground Space Technology, 2005, 20(3): 213−221
30. Zaheri M, Ranjbarnia M, Dias D, Oreste P. Performance of segmental and shotcrete linings in shallow tunnels crossing a transverse strike-slip faulting. Transportation Geotechnics, 2020, 23: 100333
31. Izadi M, Bargi K. Improvement of mechanical behavior of buried pipelines subjected to strike-slip faulting using textured pipeline. Frontiers of Structural and Civil Engineering, 2019, 13(5): 1105−1119
32. Zhao K, Chen W, Zhao W, Yang D, Song W. Study on parameters of articulated design of tunnel lining under reverse fault dislocation. Journal of Rock Mechanics and Engineering, 2018, 37: 3411−3421
33. Wang Z Z, Jiang Y J, Zhu C A. Seismic energy response and damage evolution of tunnel lining structures. European Journal of Environmental and Civil Engineering, 2019, 23(6): 758−770
34. Baziar M H, Nabizadeh A, Lee C J, Hung W Y. Centrifuge modeling of interaction between reverse faulting and tunnel. Soil Dynamics and Earthquake Engineering, 2014, 65: 151−164
35. Cui G, Wang X. Model test study on the antibreaking technology of reducing dislocation layer for subway interval tunnel of the stick-slip fracture. Advances in Civil Engineering, 2019, 2019: 1−9
36. Ranjbarnia M, Zaheri M, Dias D. Three-dimensional finite difference analysis of shallow sprayed concrete tunnels crossing a reverse fault or a normal fault: A parametric study. Frontiers of Structural and Civil Engineering, 2020, 14(4): 998−1011
37. Liu X, Li X, Sang Y, Lin L. Experimental study on normal fault rupture propagation in loose strata and its impact on mountain tunnels. Tunnelling and Underground Space Technology, 2015, 49: 417−425
38. Chen J, Liu P, Liu L, Zeng B, Zhao H, Zhang C, Zhang J, Li D. Anchorage performance of a modified cable anchor subjected to

different joint opening conditions. Construction & Building Materials, 2022, 336: 127558

39. Tao Z, Wang Y, Zhu C, Xu H, Li G, He M. Mechanical evolution of constant resistance and large deformation anchor cables and their application in landslide monitoring. Bulletin of Engineering Geology and the Environment, 2019, 78(7): 4787−4803
40. Wang X, Xu P, Wu Z, Shi J. A novel anchor method of FRP cable for long-span cable-supported bridges. In: Proceedings of the 20th International Conference on Composite Materials. Copenhagen: Aalborg University Press, 2015
41. Ma K, Tang C a, Li L, Li H, Xu N, Xiao P, Yang J. Reinforcement effects of anti-shear gallery of Dagangshan right bank slope based on microseismic monitoring and numerical simulations. Journal of Rock Mechanics and Engineering, 2013, 32(6): 1239−1247
42. Ning Y U, Weiya X U, Wentang Z, Anchi S H I, Guanye W U. Reinforcement effect analysis and global safety evaluation of arch dam and abutment of Baihetan hydropower station. Journal of Rock Mechanics and Engineering, 2008, 27(9): 1890−1898
43. Xiang B, Jiang Q, Song S, Zhou Z, Zhou C. Reinforcement design method for deep embedded concrete shear resistance structure and its application to large scale engineering slope. Journal of Rock Mechanics and Engineering, 2012, 31(2): 289−302
44. Li W, Kang H, Jiang Z, Si L, Cai R, Guo G. Deformation failure mechanism of fractured deep coal-rock mass and high-pressure grouting modification strengthening testing. Journal of China Coal Society, 2021, 46(3): 912−923
45. Liu R, Zheng Z, Li S, Yang H. Mechanical properties of fractured rock mass with consideration of grouting reinforcement. China Journal of Highway and Transport, 2018, 31(10): 284−291
46. Zhang J P, Liu L M, Liu C X, Sun D l, Shao J, Li Y. Research on mechanism of bolt-grouting reinforcement for deep fractured rock mass based on prestressed anchor and self-stress grouting. Rock and soil mechanics, 2020, 41(11): 3651−3662
47. Tao Z G, Zhu C, He M C, Karakus M. A physical modeling-based study on the control mechanisms of negative Poisson's ratio anchor cable on the stratified toppling deformation of anti-inclined slopes. International Journal of Rock Mechanics and Mining Sciences, 2021, 138: 104632
48. Tao Z, Luo S, Qiao Y, He M. Key factors analysis and constitutive equation modification of a macro-NPR bolt for achieving high constant resistance and large deformation characteristics. International Journal of Rock Mechanics and Mining Sciences, 2021, 147: 104911
49. He M, Li C, Gong W, Wang J, Tao Z. Support principles of NPR bolts/cables and control techniques of large deformation. Journal of Rock Mechanics and Engineering, 2016, 35(8): 1513−1529
50. Lai B, Liew J Y R. Investigation on axial load-shorting behaviour of high strength concrete encased steel composite section. Engineering Structures, 2021, 227: 111401
51. Lai B, Liew J Y R, Hoang A L. Behavior of high strength concrete encased steel composite stub columns with C130 concrete and S690 steel. Engineering Structures, 2019, 200: 109743
52. Riedel P, Leutbecher T, Piotrowski S, Heese C. Effect of specimen geometry on the compressive strength of ultra-high performance concrete. Beton-und Stahlbetonbau, 2018, 113(8): 598−607
53. Liu Q, Lei G, Peng X, Lu C, Wei L. Rheological characteristics of cement grout and its effect on mechanical properties of a rock fracture. Rock Mechanics and Rock Engineering, 2018, 51(2): 613−625
54. Lee J S, Bang C S, Mok Y J, Joh S H. Numerical and experimental analysis of penetration grouting in jointed rock masses. International Journal of Rock Mechanics and Mining Sciences, 2000, 37(7): 1027−1037
55. Ma K, Tang C A, Liang Z Z, Zhuang D Y, Zhang Q B. Stability analysis and reinforcement evaluation of high-steep rock slope by microseismic monitoring. Engineering Geology, 2017, 218: 22−38
56. Yan X, Sun Z Z, Li S C, Liu R T, Zhang Q S, Zhang Y M. Quantitatively assessing the pre-grouting effect on the stability of tunnels excavated in fault zones with discontinuity layout optimization: A case study. Frontiers of Structural and Civil Engineering, 2019, 13(6): 1393−1404
57. Liu X. Study on the displacement patterns subjected to active fault slip along the axial of deep buried tunnel. Rock and soil mechanics, 2021, 42(5): 1304−1312
58. Liu X, Zhang C, Xiao H, Zhou H, Chi F. Deformation and failure characteristics of a deeply buried tunnel subjected to creep slip fault movement: Based on the engineering conditions of Yunnan water intake project. Bulletin of Engineering Geology and the Environment, 2022, 81(8): 322